

# Sound-speed measurements in the surface-wave layer

Eric Terrill and W. Kendall Melville

*Scripps Institution of Oceanography, University of California, San Diego, La Jolla, California 92093-0230*

(Received 28 January 1997; revised 21 July 1997; accepted 23 July 1997)

Wave breaking at the surface of the ocean entrains bubbles, significantly modifying the phase speed and attenuation of acoustic waves propagating through the resulting two-phase medium. An autonomous buoy system was developed that directly measures sound speed at 3.33, 5, and 10 kHz at seven depths ranging from 0.7 to 7 m through the use of a travel-time technique. Simultaneous measurements at each depth are obtained at a 2-Hz rate, allowing observation of the unsteady sound-speed field from individual bubble injection events, as well as the calculation of mean sound speeds. The travel-time technique allows a direct measurement of the sound speed, eliminating the uncertainties common with inferring sound speeds from bubble population data. The sound speed buoy was deployed in the North Atlantic during the winter of 1993–94 as part of the Acoustic Surface Reverberation Experiment (ASREX). Our aim was to characterize the highly variable near-surface sound-speed field under varying environmental conditions. Forty-three days of data were obtained spanning several storm cycles with wind speeds and significant wave heights reaching 20 m/s and 8 m, respectively. During periods of intense wave breaking, average sound speeds below 1000 m/s were observed at the 0.7-m measurement depth while instantaneous sound speeds during individual events approached values as low as 300 m/s. Furthermore, the data suggest that the dispersive effects of bubbles may extend to frequencies as low as 5 kHz near the surface during storms. Strong correlations of the mean and rms sound speed with the overlying wind and wave fields were found. © 1997 Acoustical Society of America. [S0001-4966(97)02711-2]

PACS numbers: 43.30.Es, 43.30.Nb, 43.30.Xm [SAC-B]

## INTRODUCTION

The study of breaking waves and the associated bubble injection has received considerable attention from acousticians and oceanographers interested in air–sea interaction. During periods of rough weather, the scales of wave breaking tend to increase with increasing sea states, vigorously mixing the surface waters and injecting bubbles into the water column. Observations of bubbles using a variety of techniques show their presence to depths of  $O(10)$  m while the bulk of the entrained air resides in the first few meters below the surface. Bubble clouds (or plumes) form as a result of wave breaking, with near-surface turbulence and Langmuir circulations contributing to their evolution.<sup>1,2</sup> Wave breaking also plays a primary role in the dissipation of energy in the wave field, transferring energy and momentum to surface currents and turbulence. This turbulence is thought to be the main source of mixing in the near-surface waters, enhancing both heat and gas transfer across the interface.

Interest in the acoustical properties of entrained bubbles has existed for a number of years, stemming from the introduction of sonar systems in World War II. Theory and observations show that bubbles can be both efficient scatters and absorbers of sound. For example, for acoustic frequencies at or near its lowest resonant frequency, a bubble has a scattering cross section  $O(1000)$  times that of a solid particle of similar dimensions. Furthermore, both individual resonances and collective oscillations of groups of bubbles are known to contribute significantly to the ambient noise spectrum of the ocean.<sup>3–7</sup> One area of recent interest has been the effect of near-surface bubbles on low-frequency scattering and reverberation from the air–sea interface. High levels of

low-frequency scatter during high wind speeds suggest that entrained bubbles near the surface change the nature of the backscatter.<sup>8,9</sup>

Methods used in the past to measure bubbles and their distributions have included both optical and acoustical techniques. Optical techniques pioneered by Johnson and Cooke<sup>10</sup> and later used by others<sup>11–13</sup> are plagued by small sampling volumes, especially for large bubbles, and the failure to identify small bubbles. However, a recent development of an optical “depth of focus” technique offers promise of resolving bubble radii ranging from 20 to 1000  $\mu\text{m}$ .<sup>14</sup> The techniques used have been slow in their sampling rates  $O(0.1)$  Hz) or of short duration  $O(30)$  min), and most require laborious processing (in some cases, manual counting). Despite the shortcomings of past optical data, the findings of Johnson and Cooke<sup>10</sup> of a slope in the bubble size distribution of  $a^{-3}$  to  $a^{-4.5}$  (for bubble radii  $a$  greater than 60  $\mu\text{m}$ ), has been incorporated into models of gas transfer and acoustic propagation.<sup>1,15</sup> Due to data storage and processing constraints, optical techniques are currently unsuitable for a remotely operated system which would be used for obtaining long time series of  $O(1)$  month) duration.

Acoustic methods of measuring bubbles are attractive because of the ability to design robust equipment for the harsh operating conditions of the surface layer and the existence of digital signal processing techniques designed for large amounts of data. Both *in-situ* and remote acoustic methods have been used in past bubble studies. The *in-situ* methods initiated by Medwin and his colleagues<sup>16–19</sup> used a variety of techniques to study bubbles and their affects on acoustics in calm conditions. Studying the scattering and ab-

sorption of sound pulses over a range of frequencies, they inferred bubble populations over time-averaged signals  $O(10$  min) in waters 3 m and deeper. Later work included the measurements of dispersive and nondispersive sound speeds. Sound speeds were calculated by measuring phase shifts in a continuous-wave signal between two fixed hydrophones. Again, this work was done in relatively deep water and under benign conditions. More recently, Medwin and his colleagues have developed a bubble resonator that measures the response of bubbles ensonified in the resonant chamber.<sup>19</sup> A drawback of this device was the long sampling period of 10 s. An excellent review of the performance of this device in the laboratory is given by Su.<sup>20</sup>

Efforts to remotely measure bubbles in the surface layer have been made by Vagle and Farmer.<sup>21</sup> Backscatter data from multifrequency, upward looking sonars was interpreted to provide bubble size distributions for radii  $\sim 10$ – $100$   $\mu\text{m}$ . Bubble size distribution slopes were reported to vary from  $-1$  to  $-8$  during 45 min of sampling. In earlier work, Farmer and Vagle<sup>22</sup> integrated over the measured bubble populations to arrive at a void fraction, defined as  $\beta = (4/3)\pi \int a^3 n(a) da$  [typically  $n(a)$  is defined as the number of bubbles per  $\text{m}^3$  per micron radii increment]. Using known relationships between low-frequency sound speed and void fraction of air in water,<sup>23,24</sup> a depth profile of the sound-speed anomaly due to air injection from breaking waves was calculated. For winds of 12 m/s during the FASINEX experiment, a sound-speed anomaly of 19.0 m/s ( $\beta \sim 10^{-6}$ ) at the surface was reported.

More recent efforts to directly measure near-surface sound speeds were undertaken in a series of field measurements by Lamarre and Melville.<sup>25,26</sup> Their direct measurements of sound speed eliminates the difficulties involved with inferring sound speeds from bubble populations or void fractions. Lamarre and Melville<sup>25</sup> pointed out that uncertainties in bubble population data, especially for large bubbles, can lead to large errors when interpreting upward looking sonar data for sound-speed profiles. The integrals used for calculating void fraction are sensitive to both the slopes of the power laws that describe the bubble size distributions and the limits of bubble sizes over which the integration is performed.

At acoustic frequencies much less than the resonant frequencies of the bubbles in the air/seawater mixture, the speed of sound is  $c_m = 1/(\rho_m K_m)^{1/2}$ , where the density and compressibility of the mixture are given by  $\rho_m = \beta \rho_a + (1 - \beta)\rho_w$  and  $K_m = \beta K_a + (1 - \beta)K_w$ , respectively. Since the density and compressibility of the mixture depend upon the amount of air entrained, the sound speed is a function of the void fraction of air. This low-frequency limit of the sound speed is given by Wood's curve shown in Fig. 1 and has been shown to be valid for sound speeds as low as 30 m/s.<sup>27</sup> It is clear that the sound speed is sensitive to void fraction with the reduction providing an excellent indication of entrained air. For example, at void fractions of  $O(10^{-4})$  the sound speed is roughly halved.

The instrument developed by Lamarre and Melville measured travel times of acoustic pulses transmitted across a horizontal pathlength of approximately 400 mm. Using a

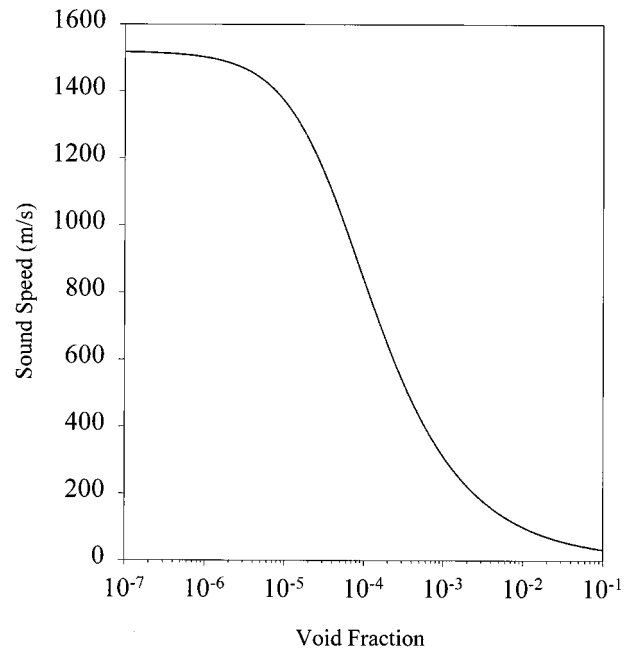


FIG. 1. Wood's curve showing sound speed as a function of void fraction.

vertical array of instruments, simultaneous measurements of sound speed were made at several depths, starting at 0.5 m and extending to 4 m, at sampling rates of 4 Hz. The high temporal resolution of the system allows observations of the changing sound-speed profile due to wave breaking.

Experiments were conducted off San Diego, California and in Buzzard's Bay, Massachusetts. For both sites, winds never exceeded 8 m/s. During the experiments, the instrument was tethered to the support ship where data acquisition and control systems were located. At a depth of 0.5 m, observations of recently generated bubble plumes produced reductions of  $O(800$  m/s) while several reductions of  $O(100$  m/s) were frequently measured during moderate wind conditions. Averages of the sound-speed reduction time series were computed for the various depths to investigate the depth dependence of the sound-speed field. For winds of 7 to 8 m/s, an exponential decrease with depth was observed in qualitative agreement with the sound-speed profiles inferred by Farmer and Vagle;<sup>22</sup> however, significant differences were found in the constants used to describe the exponential fit. Attempts at parametrizing the average sound-speed reductions with the wind speed offered some correlation but significant scatter in the data suggested the need for a larger data set.

Lamarre and Melville extended the measurements to include simultaneous sound-speed measurements at multiple frequencies from 5 to 40 kHz. A broadband pulse was band-pass filtered at various frequency bands, allowing travel-time and attenuation measurements to be made at the various bands. In the 8-m/s winds, the sound speed was observed to be nondispersive at frequencies below approximately 20 kHz.

In Sec. I of this paper, an autonomous buoy system designed for long-term sound-speed measurements in the surface wave zone is described. Section II describes the ASREX field experiment. Section III summarizes the quality of the

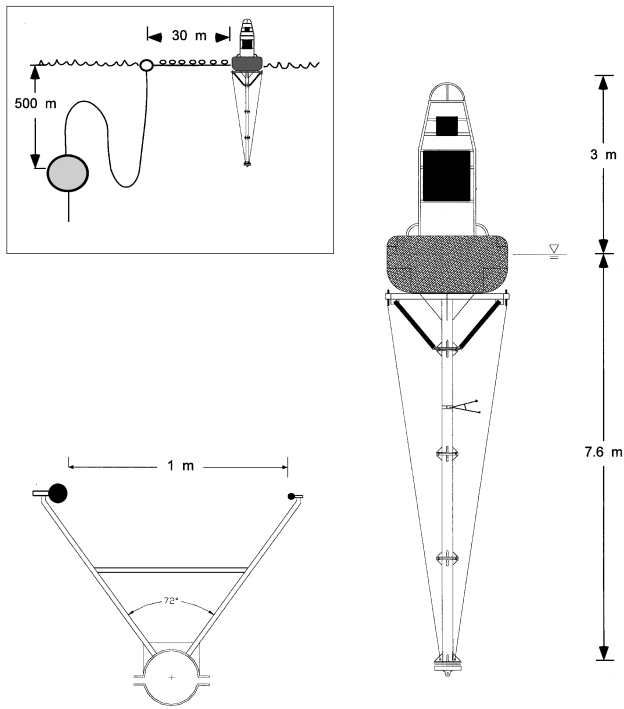


FIG. 2. Schematic of the sound-speed buoy system. Insets include the inverse catenary of the deep water mooring and a plan view of the sound-speed modules which affix to the spar of the buoy.

data and establishes error bounds on the measurements. Section IV consists of analyses of the mean and rms sound speeds in the context of the environmental parameters measured during the experiment. In Sec. V the fine scale properties of the sound-speed field are examined, providing insight into the variability of the near-surface layer. Section VI concludes the paper with a discussion of the results obtained from the analysis.

## I. EQUIPMENT DESCRIPTION

A buoy was designed to support the acoustic instrumentation under a wide range of sea states. The resulting structure has an overall length of 10.7 m with a maximum diameter of 2.44 m at the waterline (see Fig. 2). It is composed of three main sections: a surface tower fabricated from stainless steel, a central buoyancy section, and a subsurface spar section. The tower provides mounting locations for solar panels, ARGOS transmitters, radar reflector, and a navigation beacon. An instrument case, housing the electronics and data acquisition system, is mounted at the base of the tower. The buoyancy is provided by a Seaward International toroid float with 2950 kg total buoyancy. The center well of the toroid is filled with a battery pack connected to both the instrument case and the solar panels. The 7-m subsurface spar, fabricated of three sections of 203-mm-o.d. aluminum tubing, is the mounting point for the sound-speed modules and other sensors. A counterweight at the bottom of the spar provides additional stability. The three sections are designed to provide ease of assembly prior to deployment and simplify shipping of the buoy when disassembled.

Full scale drifter tests of the buoy system and its various components were carried out off Pt. Conception, California in an attempt to match the severe conditions expected in an Atlantic winter. Video studies of the buoy motion in 3.6-m seas revealed the buoy followed the longer waves (periods of 8 s and greater) with heave around  $\pm 10$  cm. In these tests, pitch and roll were limited to approximately  $15^\circ$ .

The travel-time technique employed on the sound-speed buoy is similar in principle to the design used by Lamarre and Melville.<sup>25,26</sup> The system was required to operate autonomously for a period of a few months, dictating some important aspects of the design: the resolution of the system is in the range of 2–5 m/s, measurements can be made simultaneously at seven discrete depths at a rate of 2 Hz, and the required computing power is relatively modest. Furthermore, the system is robust, a requirement for extended operation in the harsh conditions of the near-surface wave-breaking zone in the North Atlantic during the winter.

Each sound-speed module is composed of a rigid A-shaped frame with a transmit and receive transducer at the base of the “A.” Extensive laboratory acoustic testing of the A-frame and spar connection was conducted to avoid structural interference with the acoustic signals. An I.T.C. model no. 1032 transmit transducer and an I.T.C. model no. 1042 hydrophone were selected because of their resonant frequencies and response levels. The two modules nearest the surface have a 0.5-m pathlength to prevent multipath problems resulting from surface reflections. The deeper modules have a nominal pathlength of 1 m. Seven modules were spaced vertically at the following depths below the water line: 0.69, 1.02, 1.58, 1.96, 2.96, 4.44, and 6.94 m. The uneven vertical spacing of the modules provides a higher vertical resolution of the sound-speed field near the water surface where the largest gradients in sound speed are expected.

The sound speed is calculated through the direct measurement of the travel time of an acoustic pulse across the pathlength between the transmit and receive transducer.<sup>25</sup> The acoustic pulse is approximately three periods of a discrete frequency. The amplitude of the pulse is windowed to prevent impulsive loading of the transducer. The pulse is sent with a center frequency of 3.33, 5, or 10 kHz. The signal received at the hydrophone is transmitted via cable to the instrument case where it is digitized and processed.

Data acquisition was performed with a DAQBOOK (IOTECH Inc., Cleveland Ohio) parallel interface data acquisition system that was connected to a Compaq 486/33 notebook computer. The DAQBOOK obtains 128 samples of both the electrical signal sent to the transmit transducer and the received acoustic signal at a rate of 50 kHz per channel. The pulse travel times are calculated via cross-correlation techniques using fast Fourier transform (FFT) methods.<sup>28</sup> The travel times are stored on the computer’s hard disk along with the received signal amplitudes.

## II. EXPERIMENT DESCRIPTION

The Acoustic Surface Reverberation Experiment (ASREX) was a multi-investigator experiment designed to examine the effects of rough weather on sea-surface scattering and reverberation at frequencies below 1000 Hz. Several

instruments were deployed at both surface and subsurface locations housing a variety of acoustic and meteorological instruments. Participants in the experiment included scientists from the Institute of Ocean Science, Canada (IOS), Scripps Institution of Oceanography (SIO), University of Miami, and Woods Hole Oceanographic Institution (WHOI). The acoustic instrumentation consisted of the University of Miami's low-frequency source and vertical line array, upward looking and sidescan sonars deployed by the IOS group, and the Scripps sound-speed buoy. Environmental conditions were monitored by two surface buoys deployed by WHOI. The first was a Seatex Wavescan buoy which measures the surface gravity wave field through the interpretation of the buoy's pitch and roll data. It is able to resolve the directional wave field over wave periods ranging from 2 to 30 s. (Seatex, Trondheim, Norway).<sup>29</sup> The second buoy was a 3-m discus buoy (similar to those used by the National Data Buoy Center) which contained a full suite of meteorological sensors including wind speed and direction, sea-surface temperature, and barometric pressure. A detailed description of the experiment, including equipment summaries, deployment procedures, sampling strategies, and personnel involved can be found in Galbraith *et al.*<sup>30</sup>

The deep water mooring for the SIO buoy was designed and built by the Woods Hole Rigging Shop for the ASREX experiment (see Fig. 2). The mooring was designed to keep the buoy secure throughout the winter yet minimize any effects the mooring may have on the buoy's ability to follow the surface waves. The instrumented buoy was moored to a subsurface float at 500-m depth through an inverse catenary which decoupled the surface buoy from the mooring during periods of high currents. A scope (the ratio of horizontal distance to depth) of 2.62 was used between the surface buoy and the subsurface float at 500 m. The mooring was connected to the buoy through the use of a guard surface float that further decoupled the mooring from the buoy. The connection between the guard float and the buoy was composed of 30-m 3/8-in. chain covered by large diameter Tygon tubing. Small floats were connected to the surface tether at intervals of approximately 0.75 m to provide buoyancy. A similar design has been used in mooring the Seatex Wavescan buoy in deep water, successfully allowing the buoy to obtain unbiased wave measurements.

The moorings were set in the Atlantic at roughly 34°N, 70°W in mid-December 1993 using the R/V KNORR operated by WHOI. Nominal water depth was 4500 m. The mooring site was chosen for the flat bathymetry which allowed accurate placement of the subsurface instruments in the water column, and for the rough weather conditions typical of an Atlantic winter. After deployment of the sound-speed buoy, observations of the buoy motion under rough conditions became available as the winds quickly rose to 50 kn and peak wave heights were estimated to reach 12 m. Video of the buoy motion again revealed a maximum pitch/roll of approximately 15° and negligible heave. After a 3 month deployment, the moorings were recovered using the R/V EDWIN LINK operated by Harbor Branch Oceanographic Institution under more favorable seas.

For the 3 month deployment, the sound-speed buoy op-

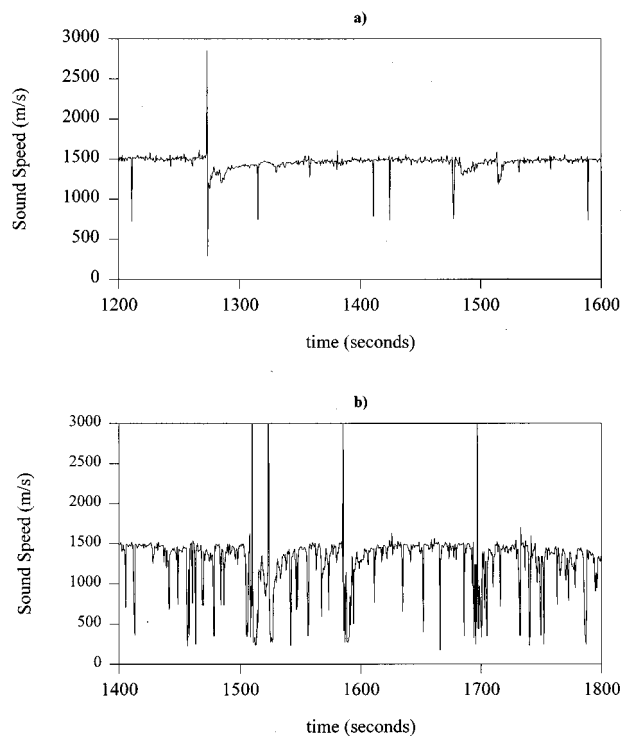


FIG. 3. Example time series of 3.33-kHz sound speed, for (a) moderate sea state ( $H_{1/3}=2.3$  m,  $U_{10}=11.2$  m/s) and (b) extremely rough conditions 13.5 h later ( $H_{1/3}=4.2$  m,  $U_{10}=12.0$  m/s). Bad data points include those that exist at values much greater than the bubble-free sound speed as well as the single points that exist near 700 m/s.

erated on a 44% duty cycle to extend the data storage capacity and battery power. The buoy operated with a schedule of 40 min on/50 min off with a travel-time measurement sample rate of 2 Hz per module. The center frequency of the acoustic pulse used for the measurement was changed at each new 40-min sampling period. Hence a 40-min time series of 3.33-kHz sound-speed data would be available every 4.5 h over the duration of the deployment. Sound-speed averages, battery voltages, and buoy position were telemetered to shore via the ARGOS system on a daily basis.

### III. DATA

#### A. Data available

Upon recovery of the buoy, it was discovered that only 43 days of data were recorded, somewhat less than the desired 3 months. Close inspection of the system voltage over the duration of the deployment showed a sudden drop from which the buoy never recovered on 21 January 1994. Post-recovery inspection of the buoy showed evidence of abrasion in one of the submerged cables, resulting in exposure of the conductors to seawater. Other nearby instruments also experienced similar cable degradation to varying degrees. This was attributed to fish bite. With the conductors grounded to seawater, the buoy's batteries drained below acceptable system operating levels.

Directional wave data from the Seatex buoy and meteorological observations from the 3-m discus were successfully obtained by WHOI over the interval of sound-speed

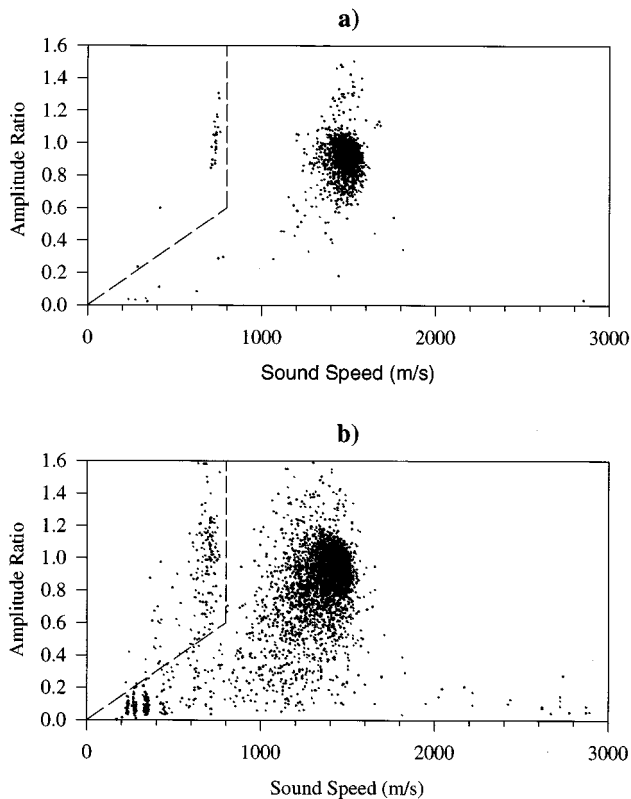


FIG. 4. Scatter plots of sound speed versus received signal amplitude for both the previously shown time series during (a) a moderate sea state and (b) rougher conditions. The dashed line is the criterion used to remove bad data points.

measurements, providing the necessary environmental measurements for comparison with our data set. The meteorological measurements show that for the 43 days of operation, seven intense storms lasting 2 to 3 days passed over the array of moorings. All storms had winds exceeding 15 m/s accompanied by significant wave heights of several meters or more.

## B. Preprocessing of acoustic data

In order to calculate the sound speed from the travel-time data, accurate measurements of the acoustic pathlength are needed for each sound-speed module. This pathlength includes any differences between the physical and acoustic centers of the transducers, and any changes in the separation of the transducers due to unforeseen incidents (e.g., fish hits). A convenient method of measuring the pathlength is to use travel-time data obtained during very calm periods, when few bubbles exist in the water column. Since the bubble-free sound speed can be accurately calculated using temperature and salinity information,<sup>31</sup> an *in-situ* acoustic pathlength may be computed during various times throughout the deployment. The acoustic pathlengths were computed using four calm periods in the 43 day record and found not to vary by more than  $O(0.001)$  m for any of the seven modules. Resolving the standard deviations of the pathlength measurements as a sound speed, the sound-speed module's error due to variations in pathlength would be approximately  $\pm 3$  m/s

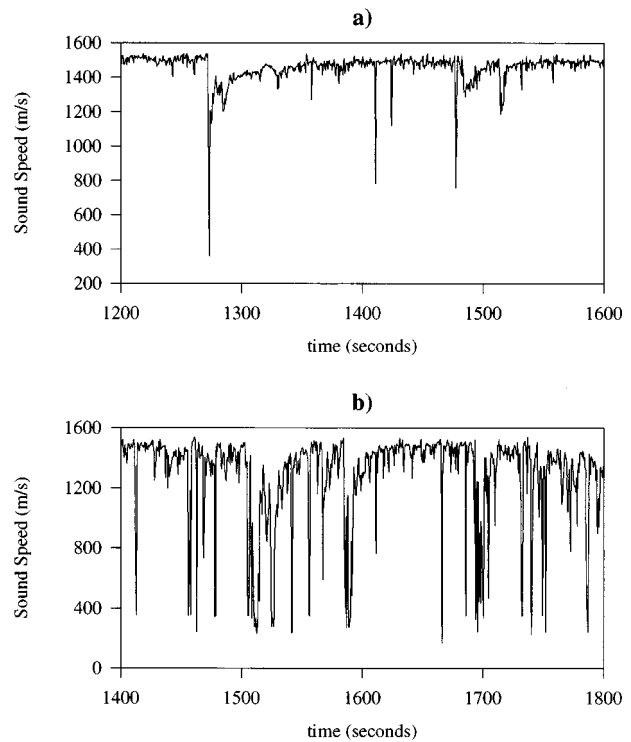


FIG. 5. The sound-speed time series of Fig. 3 after the bad data points are removed and replaced with the average of the neighboring points. Again, (a) is the moderate sea state and (b) is the rougher conditions.

over the course of the measurements. These uncertainties are similar in magnitude to the resolution of the system due to sampling rates of the acoustic signals.

As with any new instrument, the quality of the sound-speed data required assessment. It was expected that during extreme weather, ambient noise and signal attenuation may cause the signal-to-noise ratio to drop below acceptable levels for accurate travel-time measurement. To what extent this would occur was unknown because of the novelty of the measurement under these extreme conditions. After examining the data for the seven depths, it appeared that data from the two shallowest measurements contained some spurious points during periods of intense breaking. Figure 3 shows two time series of 3.33-kHz sound-speed data measured at 0.7 m during a storm event. Time series (a) is representative of the sound speed during a moderate sea state ( $H_{1/3} = 2.3$  m,  $U_{10} = 11.2$  m/s) while time series (b), obtained 13.5 h later, represents much rougher conditions ( $H_{1/3} = 4.2$  m,  $U_{10} = 12.0$  m/s). Two features present in both time series, thought to be bad data points, are the isolated points at levels much greater than the bubble-free sound speed ( $\approx 1500$  m/s) as well as single data points that seem to occur near 700 m/s.

Some insight into recognizing bad data points of the time series is possible if scatter plots are made of the sound speed against the ratio of the amplitude of the received to transmitted signal. Figure 4 shows the corresponding scatter plots for the time series in Fig. 3. Three distinct clusters appear in the two plots: good data consisting of the majority of the points and two groupings of questionable data resulting from different mechanisms. The first grouping of bad

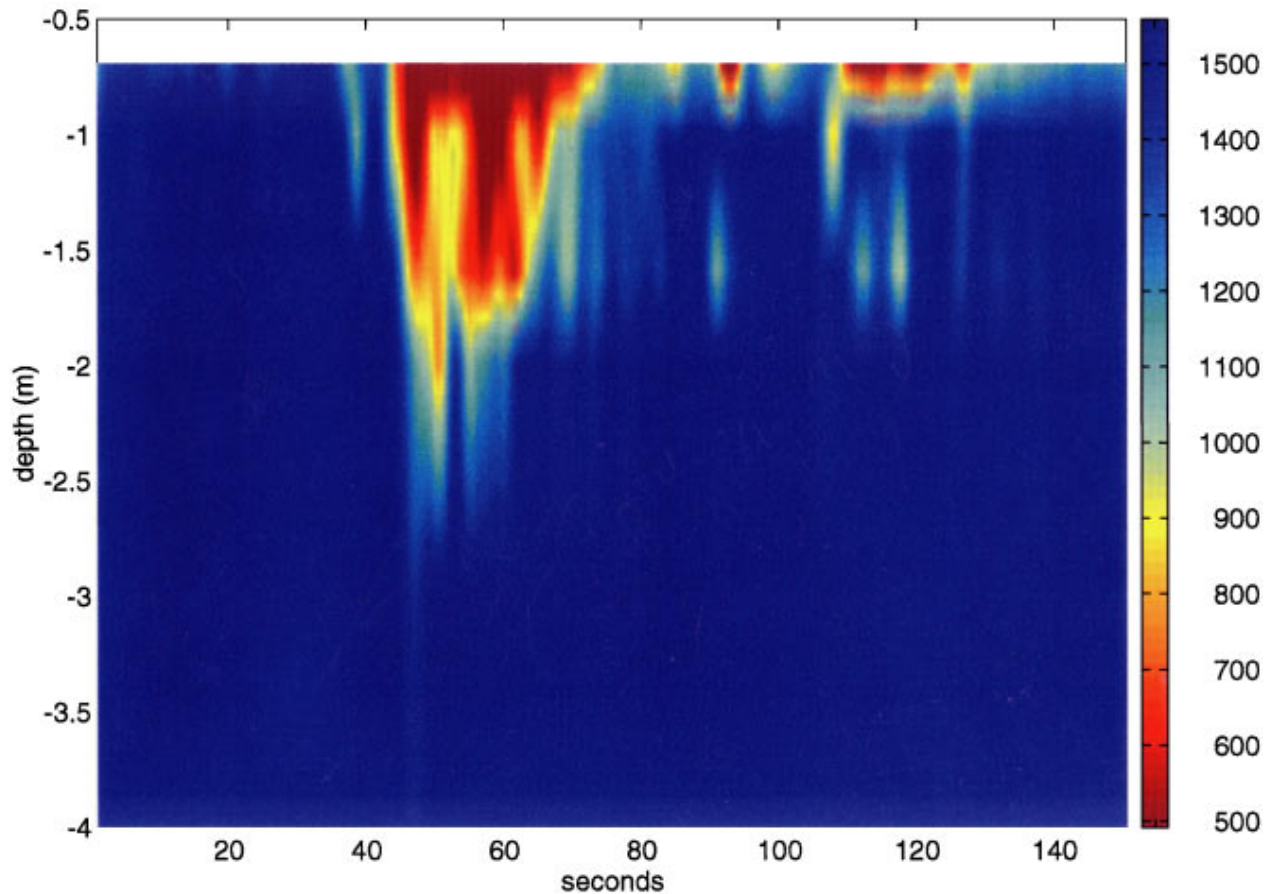


FIG. 6. Color contour plot of the response of the sound-speed field to a large single event. A region of very low sound speed exists near the surface for  $O(30)$  s while at depth, the reductions are smaller and last for shorter periods of time. The high-frequency oscillation visible in the figure is attributed to orbital motions of the waves advecting the bubble cloud past the sensors.

data is composed of the points of very large sound speed but with small amplitude. These points are attributed to a low signal-to-noise ratio (SNR), i.e., the signal level is too low for the cross correlation to effectively find the arrival time of the transmitted acoustic wave. If the transmitted acoustic pulse is masked by ambient noise or attenuation, low-level electrical cross talk between the transmit and receive transducer cables may be cross correlated, resulting in very short travel times (large sound speeds).

The second group of the bad data points are those that appear shifted  $\sim 700$  m/s from the central cluster of good points. These points occur because the peak of the cross correlation is shifted in time by one period in the three period acoustic pulse. The resulting calculated sound speed is then

$$C = \frac{L}{T + T_\lambda}, \quad (1)$$

where  $T_\lambda$  is the period of one 3.33-kHz wavelength. Using scatter plots of sound speed and amplitude over the 43 days of data, an empirical criterion for bad data points was arrived and that effectively separates the bad data results from the erroneous phase shifting. The dashed lines shown in Fig. 4 show boundaries by which good data is separated from bad data. The criteria were empirically selected after analyzing

similar scatter plots over the 43 day record. Careful examination of the bad data points reveals that they usually are single-point anomalies in the 2-Hz data (i.e., they are discontinuous with their neighboring points), providing confidence in the criterion used to identify bad data. Once the bad data points are identified, they are replaced with the average value of their neighbors, providing a gap-free data set (Fig. 5).

A final feature present in the scatter plots of Fig. 4 that deserves mention are the groupings that begin to appear near 360 m/s. These data points are found to exist during large events of sound-speed reduction, lasting for several seconds before the measured speeds begin to rise, presumably reflecting the presence of high void fractions and subsequent degassing. The groupings arise as a consequence of the acoustic pulse delayed beyond the width of the analog-to-digital sample window, resulting in the received pulse being clipped in time. When this occurs, the time delay which results from the cross-correlation peak may result in erroneous values. Grouping arises from the cross-correlation peak shifting by  $2\pi$ , dependent on the integral number of wavelengths the pulse is delayed outside the window.

In light of previous laboratory work, it is not surprising that the near-surface measurements are reduced to levels below 360 m/s, which corresponds to void fractions in excess

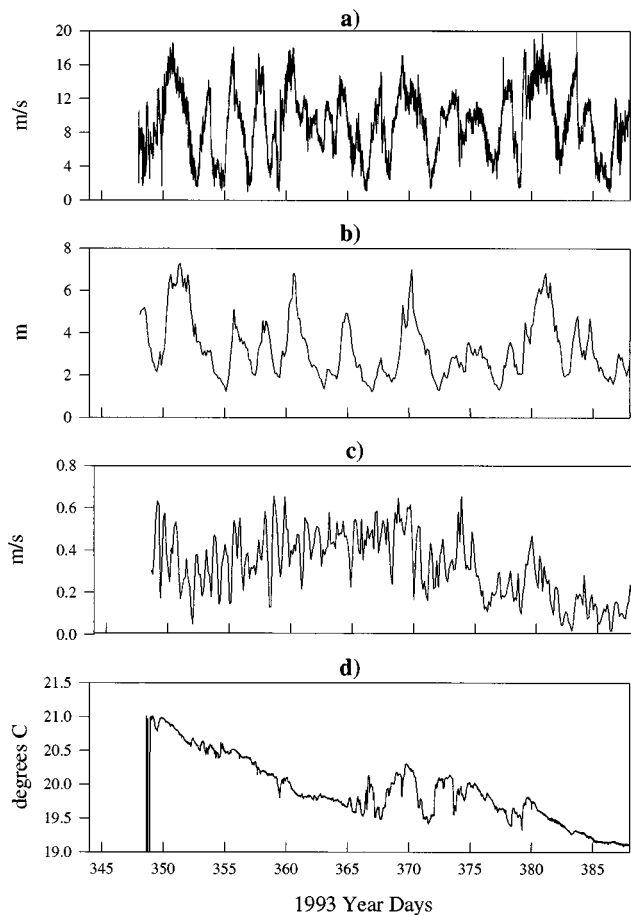


FIG. 7. Time series of the environmental conditions while the sound-speed buoy was operational: (a) Wind speed corrected to 10-m height. (b) Significant wave height. (c) Surface currents measured at 5-m depth. (d) Sea surface temperature measured at 1-m depth.

of  $10^{-3}$ . Lamarre and Melville<sup>24</sup> show that void fractions can exceed 50% for short periods directly beneath a laboratory generated wave. Similarly, it is likely that void fractions would approach or exceed 50% for short periods of time in the immediate vicinity of large breakers considering the extreme weather encountered during ASREX. To resolve the effects of the instrumentation's inability to measure very low sound speeds on the calculated mean sound speeds, conservative error bounds are set based on Wood's curve and the instrument's sample window. An upper bound is set if the ambiguous data points below 360 m/s are conservatively set equal to the 360-m/s level that is confidently resolved. The lower bound is set based on assuming that the lowest values the ambiguous points would approach is the lower limit of Wood's curve: at high void fractions of approximately 50% a sound-speed minimum exists at 20 m/s. The minimum reflects the influence of the mixture's density on the sound speed at high void fractions. At very high void fractions, the curve approaches the sound speed of air. For the rough sea state conditions shown in Figs. 3(b), 4(b), and 5(b), the resulting range of mean sound speeds bounded by these limits is 1284–1299 m/s, a 1% error in the mean sound speed and a 6% uncertainty in the mean sound-speed reduction.

As expected, the uncertainty of the mean sound speed is related to the quantity of data that exceeds the lower limit of

the sound velocimeter over the course of a measurement cycle, which in turn, is dependent on the sea state and measurement depth. Typically at the 0.7-m measurement depth during rough weather, uncertainty in the mean reduction is 10–20 m/s or  $O(5)\%$ . The next measurement depth at 1 m typically contains  $O(1)\%$  uncertainty while the deeper measurements always contained much less than 1% bad data, resulting in negligible uncertainty of the mean reduction. For the remainder of this paper, the reported mean sound speeds at the shallowest depths are the larger (more conservative) of the two values (the smaller mean reduction).

While the average data reflect the results of rough weather on the sound-speed field, they do little to show how the field responds to individual breaking events. Figure 6 shows a color contour plot of the sound-speed field in the presence of a large bubble cloud that resulted from a nearby breaking wave. Time in seconds is shown on the horizontal axis, depth in meters is represented on the vertical axis, and sound speed is represented by color. Pixels between the seven measurement depths have been linearly interpolated to arrive at a smoothed figure. For this particular event, the sound speed is drastically reduced at the surface to  $O(500)$  m/s for 30–40 s. A few meters deeper, reductions of  $O(100)$  m/s appear but tend to last for shorter time periods. It is short-lived events like the one shown (also visible in later figures) that are primarily responsible for injecting air into the water column and lowering the mean sound speeds.

#### IV. PROCESSED DATA: 40-MIN AVERAGE SOUND SPEEDS

##### A. 3.33-kHz data summary

Successful operation of the sound speed buoy for 43 days provides data for analysis over a wide range of environmental conditions. Figure 7 presents time series of wind speed, significant wave height, surface currents, and sea surface temperature measured at the directional wave buoy and the 3-m meteorological buoy. Figure 8 shows the 40 min average sound speed for 3.33 kHz at the seven different depths along with significant wave height. The sea surface temperature, measured at 1 m is also plotted with the deepest sound-speed measurement.

It is apparent that the layer of water near the ocean's surface exhibits large gradients in sound speeds. Near the surface, average sound speeds routinely drop to approximately 1200 m/s, in contrast to the 7-m depth, where the average sound speed appears to follow secular trends in the temperature field. The average data also depicts the variability that exists in the near-surface sound-speed field from one storm to another. This is exemplified by the suppressed response of the sound-speed field for the storm that occurs year day 380, 1993 in comparison with the storm that occurs just ten days earlier on day 370. Note that both storms have similar peak wind speeds and significant wave heights.

##### B. Average sound-speed dependence on environmental parameters

If the presence of air in the near-surface waters is due to wave breaking, we need to consider which environmental

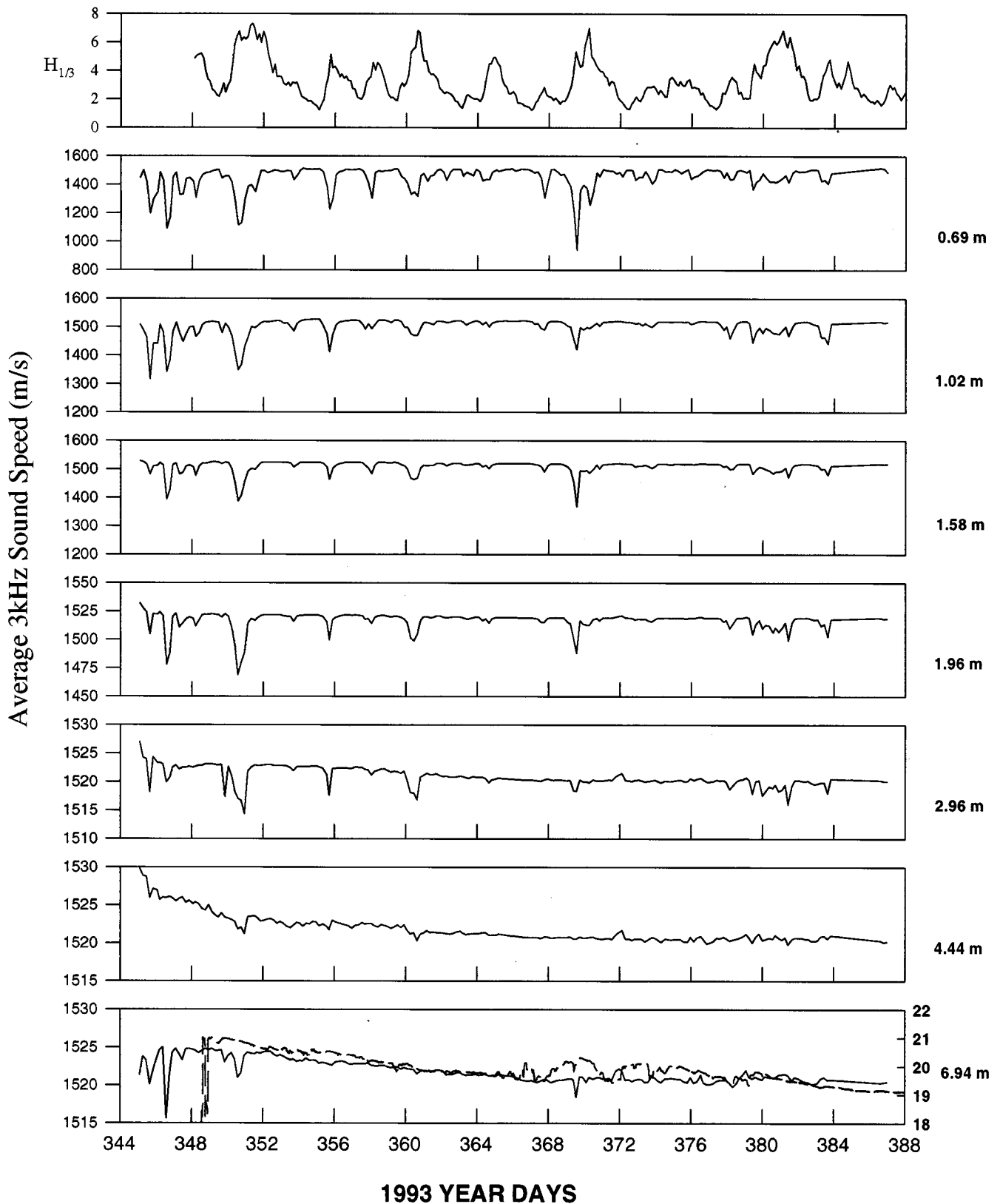


FIG. 8. Time series of the mean 3.33-kHz sound speeds measured at the seven measurement depths for the duration of the deployment. Time series of significant wave height are provided to note the locations of storms. Sea surface temperature is plotted with the deepest measurement depth to show similar trends. Note the varying y-axis scale for the different measurement depths.

conditions control deep-water wave breaking. Historically, the wind speed and significant wave height have been used for obtaining correlations with bubble-driven acoustic phenomena such as backscatter and ambient noise, with limited

success. In a comparison of ambient noise with surface wave variables, Felizardo and Melville<sup>32,33</sup> point out that the presence of swell can significantly alter the measured significant wave height while only contributing second-order effects to

the wave breaking, or the acoustically active portion of the wave field. Their work suggests that other parameters exist that better represent the intensity of wave breaking in the surface wave field. These include the wave slope and dissipation of energy of the surface wave field. The average sound-speed reductions obtained in ASREX are compared with both the classical environmental parameters of wind speed and significant wave height as well as with parameters which better describe the dynamics of the sea surface.

Figure 9(a) and (b) compares the average sound-speed reductions with the average wind speed, corrected to 10-m height, and the significant wave height. Averages are calculated from 40 min time series of data obtained from the sound-speed modules located at depths of 0.7 and 1.6 m. The two depths are selected because the shallowest measurement is in the most active region of the water column and the deeper depth is representative of the mid-depth signal of the bubbly layer. As expected, correlations exist between the average sound speeds and the wind and wave field, albeit with significant scatter.

At windspeeds less than 8 m/s, the near-surface measurement at 0.7 m appears to be independent of the wind-speed while the deeper measurement appears to be sensitive across a wider range of windspeeds. The figures reflect the variability in the shallow entrainment of air, particularly at lower wind speeds. Figure 9(b) presents a comparison of the mean reductions with the significant wave height. While a coupling of the wave field to the wave breaking process is suggested by the trends, the scatter suggests a need for a better descriptor based on the wave field. In reality, the rate and intensity of surface wave breaking, which controls the quantity of air injected, will be governed by a complex combination of environmental conditions that contribute to the sea state.

Laboratory experiments by Rapp and Melville<sup>34</sup> and Loewen and Melville<sup>35</sup> have suggested that the slope of the wave field can be used as an indicator of the strength of breaking. Furthermore, their results suggest that the steepness of the field may reflect the levels at which other related dynamic processes are occurring. This includes the associated momentum flux, mixing, and dissipation of the surface waves, as well as acoustic phenomena related to wave breaking such as ambient noise generation. Felizardo and Melville's<sup>32</sup> field measurements support the laboratory experiments by showing strong correlations of ambient noise in various frequency bands with the steepness of the wave field. Using a four wire wave gauge array, Felizardo and Melville<sup>32</sup> computed time series of the slope of the wave field from the finite difference of wave elevation between wires in the array. Comparisons of rms slope with measured ambient noise levels show a strong correlation over the 0–12 m/s wind speeds encountered over the course of that experiment.

In light of the previous results, it is useful to derive an estimate of the steepness of the wave field during the ASREX experiment. Unfortunately, the wave measurements were obtained using a pitch–roll buoy, providing no direct measurement of the wave slopes. In order to arrive at a first-order estimate of the steepness of the wave field, information

from the surface displacement power spectra is used. The power spectra of the surface elevation  $\Phi(\omega)$  can be converted to a slope spectrum  $B(\omega)$  through the linear dispersion relationship. Assuming the dispersion relation  $\omega^2 = gk$ , the corresponding slope spectrum is

$$B(\omega) = \frac{\Phi(\omega)\omega^4}{g^2}. \quad (2)$$

The slope spectrum is then integrated over a range of frequencies to arrive a parameter,

$$S_p = \int_{\omega_1}^{\omega_2} B(\omega) d\omega, \quad (3)$$

that is a measure of the steepness of the wave field. The low-frequency limit is set to correspond to 15-s waves, ensuring that the majority of the wind–wave spectrum is incorporated into the integral. The high-frequency limit of the integral is set to wave periods of 3 s, corresponding to the upper frequency limit at which the pitch–roll buoy appeared to accurately resolve the surface waves. Figure 9(c) shows the comparison of the slope parameter with the average sound-speed reduction, again for the 0.7- and 1.6-m depth measurement. The figure highlights the better correlations this parameter provides with the sound-speed reductions when compared to the significant wave height comparisons of Fig. 9(b). While the value of the slope parameter  $S_p$  does vary with the limits of integration, the resulting trends are insensitive to the integration limits if the frequency range covers the wind/wave spectrum.

The final parameter used for comparison with the sound-speed data is an estimate of the energy dissipated by the surface wave field. In the work of Felizardo and Melville,<sup>32</sup> estimates of the energy dissipation of the surface field<sup>36–38</sup> are found to correlate well with the portion of the ambient noise spectrum that results from wave-injected bubbles. If the energy dissipation of the surface wave field is due to wave breaking, it is expected to correlate with sound-speed reductions due to air injection. Earlier work by Melville *et al.*<sup>39</sup> and Loewen and Melville<sup>35</sup> in the laboratory and Kennedy<sup>40</sup> in the field produced results showing that the sound radiated by breaking scales with the energy dissipated by wave breaking.

To investigate the dissipation term, an existing model is used which is based on bulk parameters. A quasi-equilibrium model proposed by Phillips<sup>36</sup> assumes a balance between the nonlinear wave interactions, wind input, and wave breaking dissipation over an equilibrium range of wave numbers. Using previous models of the wind input and nonlinear transfers, he showed that the spectral rate of energy loss from the waves (within the equilibrium spectral range) was given by  $\epsilon(k) = \gamma\beta^3(\cos\theta)^{3p}u_{*a}^3k^{-2}$ , where  $\gamma$ ,  $\beta$ , and  $p$  are numerical constants,  $\theta$  is the included angle between the wave-number vector  $k$  and the wind vector, and  $u_{*a}$  is the friction velocity of the air flow over the water surface. Integrating over a range of wave numbers with a lower limit at the peak of the wave spectrum and an upper limit (high-frequency waves)

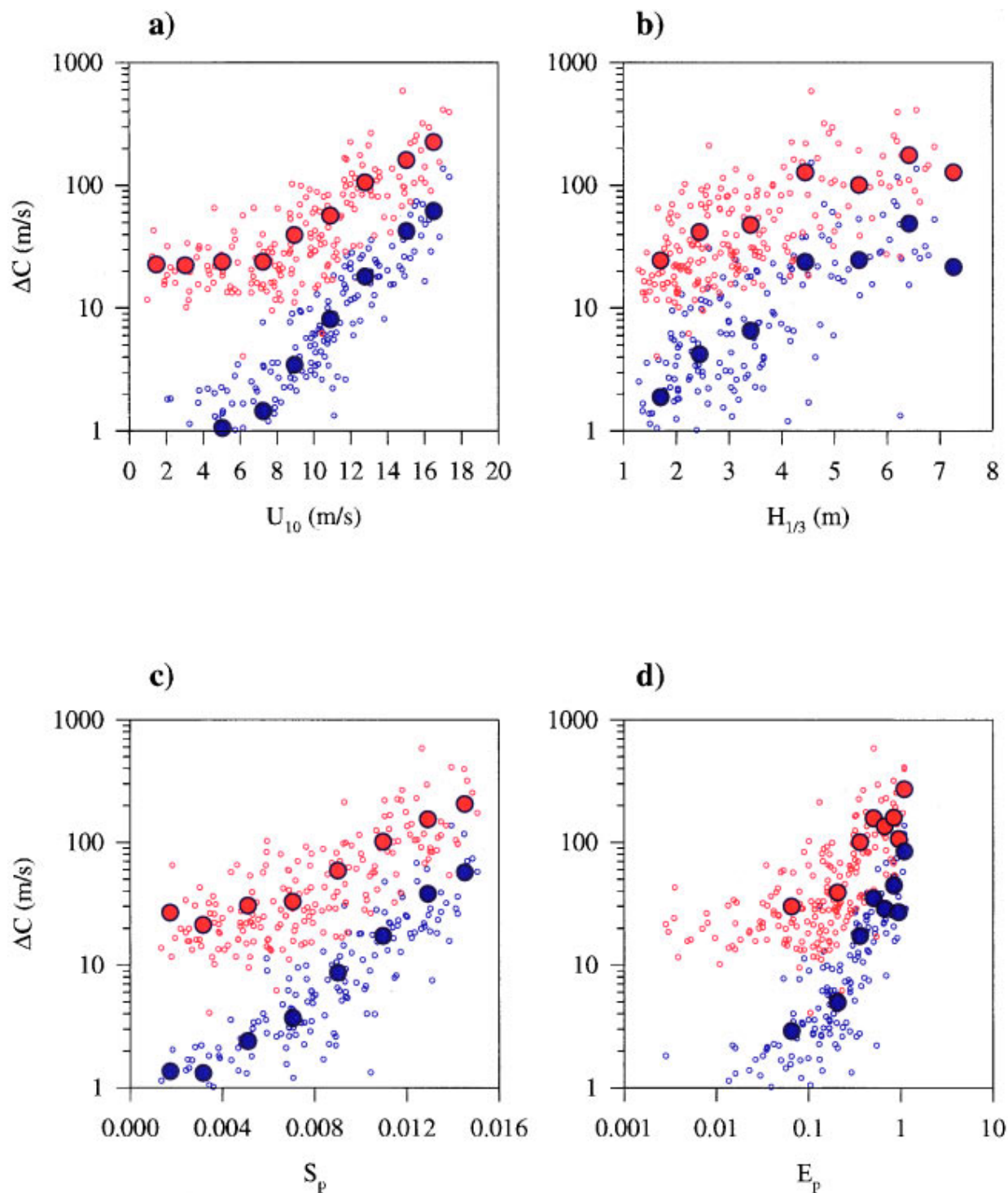


FIG. 9. Comparisons of the mean sound-speed reductions with (a) wind speed corrected to 10 m above the sea surface, (b) significant wave height, (c) computed slope parameter, (d) Phillip's (Ref. 36) bulk dissipation estimate. Data from the 0.7- and 1.6-m measurement depths are represented by the colors red and blue, respectively. Solid circles represent averages of the data grouped with the following binwidths: (a) 2 m/s, (b) 1 m, (c) 0.002, (d) 0.01.

which is determined by suppression of waves due to the presence of wind drift, a bulk estimate of the dissipation of the wave field arises and is given by

$$D = 2\gamma\beta_3 I(3p)\rho_w u_*^3 \ln \left[ r \left( \frac{c_p}{u_*} \right)^2 \right]. \quad (4)$$

Felizardo and Melville<sup>31</sup> showed that the range of the numerical constants  $\gamma\beta^3 I(3p)$  is  $3.7\text{--}8.0 \times 10^{-4}$ ; a factor of

approximately 2. The advantage of comparing this equation with measured values of entrained air is that the dissipation estimate is based not only on the wind speed (friction velocity  $u_*$ ) but the wave age  $c_p/u_*$ , which incorporates information about the surface wave spectrum ( $c_p$  is the speed of the waves at the peak of the wave spectrum). Hence the bulk estimate of the energy loss of the wave field that is important to wind-wave modeling<sup>41</sup> provides a parameter that is de-

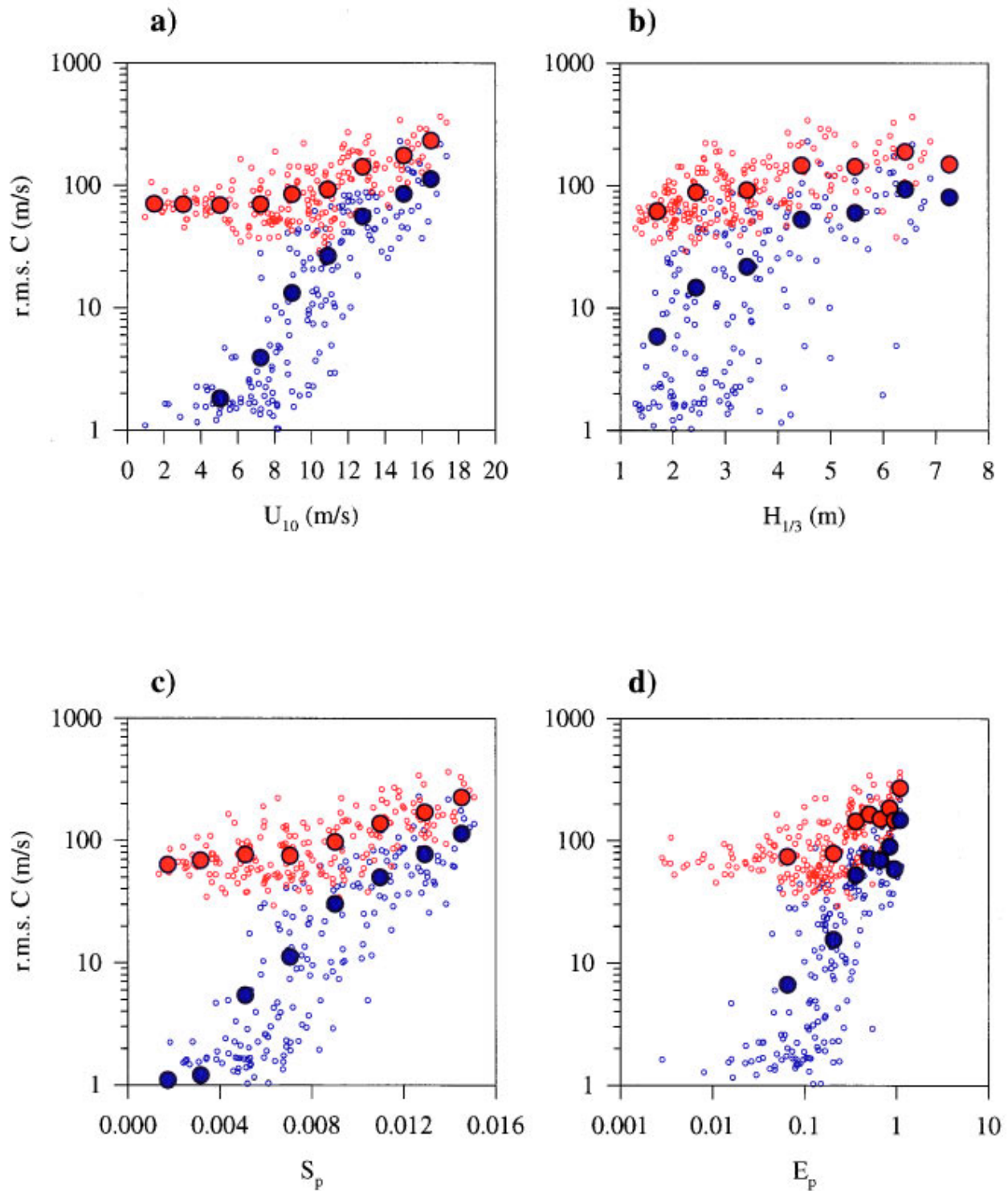


FIG. 10. Comparisons of the rms sound speed with (a) wind speed corrected to 10 m above the sea surface, (b) significant wave height, (c) computed slope parameter, (d) Phillip's (Ref. 36) bulk dissipation estimate. Data from the 0.7- and 1.6-m measurement depths are represented by the colors red and blue, respectively. Solid circles represent averages of the data grouped with the following binwidths: (a) 2 m/s (b) 1 m, (c) 0.002, (d) 0.01.

pendent on both the wind and wave conditions which can be compared with measurements of bubble-driven acoustic phenomena.

Dissipation estimates based on the wind and wave conditions during the ASREX experiment have been computed and compared with the 40-min average sound-speed deviations at both 0.7- and 1.6-m measurement depth, as is shown

in Fig. 9(d). It becomes evident that the average sound speed correlates with the dissipation estimate. While the scatter in the data suggests room for improvement in the dissipation estimate, it provides a rational means by which environmental variables are combined to arrive at a description of the intensity of wave breaking at the ocean's surface. The scatter is not surprising in light of the fact that the dissipation term

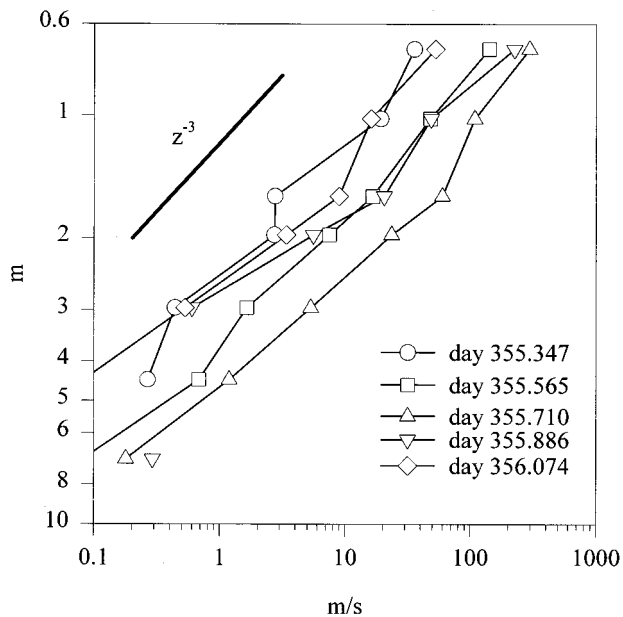


FIG. 11. Depth profiles of the mean sound-speed reduction measured over the course of a storm that began 1993 year day 355. Note that all profiles vary approximately as  $z^{-3}$ .

is the least understood of the terms in the radiative transfer equation<sup>36,41-43</sup> and presently does not include the effects of swell and wave-current interactions. It is expected that improved formulations of the dissipation function would improve the acoustic comparisons. Nevertheless, the dissipation estimate provides a descriptor of the ocean's surface which has a sound physical basis for comparison with acoustic observations.

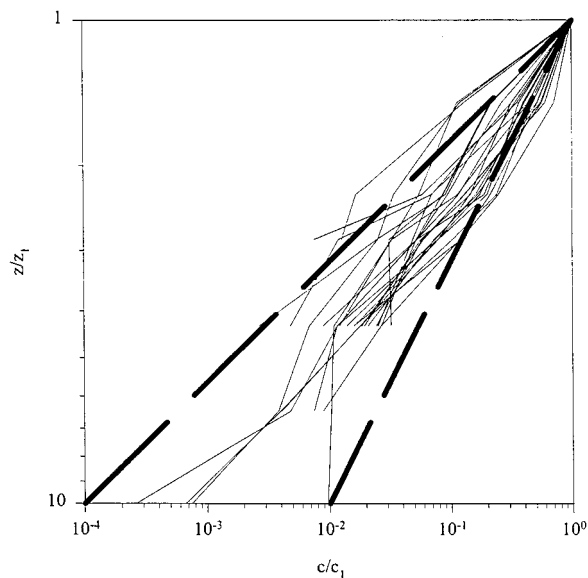


FIG. 12. Several example mean sound-speed reduction depth profiles for rough conditions measured over the course of the experiment. The profiles are normalized by the depth and mean sound speed of the shallowest measurement. Power law slopes of  $-2$  and  $-4$  are given by the heavy dashed lines.

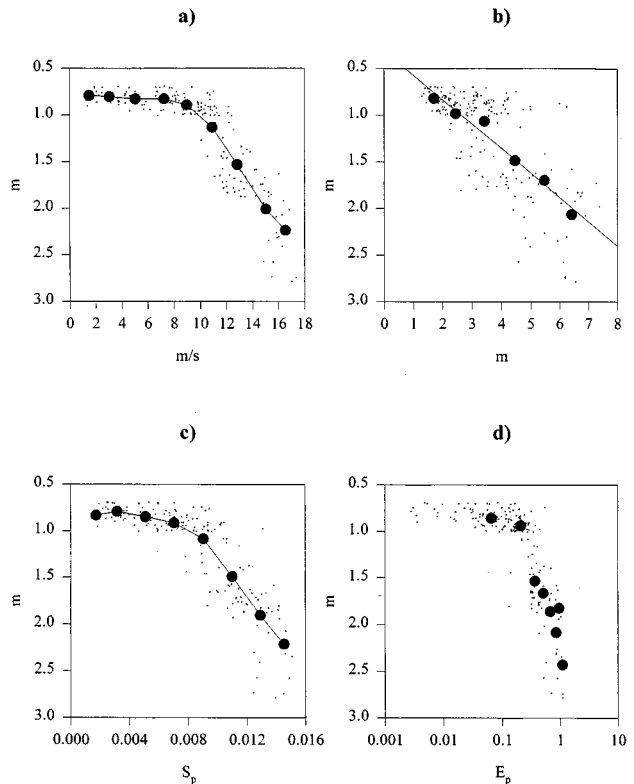


FIG. 13. The depth representing the level at which the mean sound speed is 99% of the bubble-free value ( $\beta \cong 10^{-6}$ ) is compared with (a) wind speed corrected to 10 m above the sea surface, (b) significant wave height, (c) computed slope parameter, (d) Phillip's (Ref. 36) bulk dissipation estimate. The solid circles represent averages of the data grouped with the following binwidths: (a) 2 m/s, (b) 1 m, (c) 0.002, (d) 0.01. Note the linear relationship between the contour depth and the significant wave height (binned).

### C. The rms sound-speed dependence on environmental parameters

The rms of the 3.33-kHz sound-speed data is analyzed in similar fashion to the mean data. Again the analysis is limited to the 0.7- and 1.6-m depth measurements. Figure 10(a) and (b) shows the rms sound speed at the two measurement depths compared with the windspeed and significant wave height. The trends that appear in the comparisons closely resemble those of the comparisons made with the mean sound-speed data (Fig. 9). Significant scatter again exists between the rms sound speed at the shallowest measurement with both the wind speed or wave height variable. Furthermore the scatter is reduced if the environmental variable is compared with the deeper measurement (note that  $\Delta C$  is plotted on a logarithmic scale). The rms sound speed is also compared with the wave steepness parameter and the wave dissipation estimate that was discussed above [Fig. 10(c) and (d)]. The strong correlations again suggest a coupling of the surface wave-field dynamics to the sound-speed field and that other parameters exist that may better describe the intensity of wave breaking.

### D. Depth dependence of average sound speed

In principle, the buoyant effects of bubbles ensure that the average sound-speed reductions will be at a maximum near the ocean's surface and monotonically decrease with

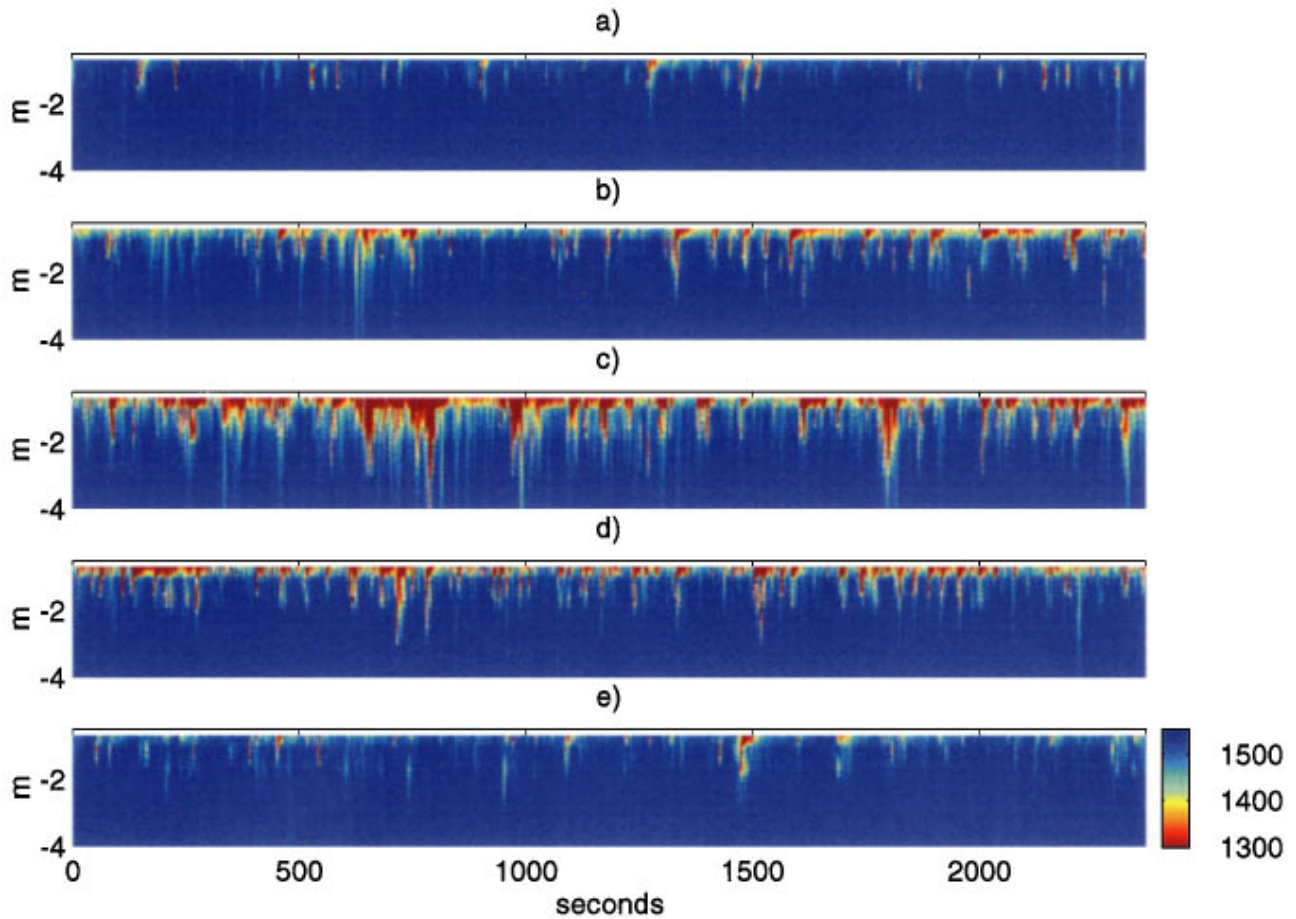


FIG. 14. Color contour plots of the 3.33 kHz sound-speed time series during a storm. Each figure is separated by 4.5 h and corresponds to the data shown in the depth profiles of Fig. 11. The 2-Hz sampled data is linearly interpolated with depth to arrive at a smoothed figure.

depth. In addition, the flux of bubbles into the surface waters increases as the incidence of wave breaking increases, further reducing the sound speed. This qualitative description of the near-surface sound-speed field has been observed in the earlier measurements of Farmer and Vagle<sup>22</sup> and Lamarre and Melville.<sup>25</sup> The large data set provided by the ASREX deployment also exhibits this trend of a decreasing sound-speed reduction depth profile, even during the roughest of conditions. Figure 11 presents the depth profiles of the mean sound-speed reductions measured over the course of a storm that began on year day 355, 1993. Each profile represents 40 min of data separated by 4.5 h. It is apparent that the average sound-speed profiles respond to the sea state, with the peak of the storm reflected in the profile with the largest sound-speed reductions.

The linear trend exhibited on the log-log scale suggests that a power-law relationship is the appropriate functional relationship for the depth dependence of the data. Furthermore, despite variations in the magnitude of the data over the course of the storm, the slope of the power-law relation appears almost constant with a value of approximately  $-3$ . This contrasts with the previous work of both Farmer and Vagle<sup>22</sup> and Lamarre and Melville<sup>25</sup> who used exponentials to describe the depth dependence of their sound-speed observations. A number of profiles spanning the 43-day record are normalized with respect to the shallowest measurement and

presented in Fig. 12. The profiles shown, which are representative of the data obtained over the course of the experiment, again exhibit power-law relations with slopes in the range  $-2$  to  $-4$ .

To explore the depth dependence of the layer of reduced sound speed, a contour representing the depth at which the mean sound speed is 99% of the bubble-free value is calculated ( $z_{0.99C_0}$ ). Its value is computed by linearly interpolating between the mean sound-speed levels at each of the seven measurement depths. The depth of the layer is compared with the various environmental parameters used to describe the mean sound-speed levels [Fig. 13(a)–(d)]. The resulting trends point towards a layer depth that increases with both the wind speed and significant wave height as well as with the estimates of wave steepness and wave energy dissipation. The data suggest a linear relationship between the depth of the reduced sound-speed layer and the significant wave height:

$$z_{0.99C_0} = 0.26H_{1/3} + 0.31 (r^2 = 0.97), \quad (5)$$

where  $r^2$  is the correlation coefficient [regression performed after binning the data according to 1-m increments in wave height, see Fig. 13(b)]. Since the significant wave height is approximately four times the wave amplitude rms,<sup>41</sup> the re-

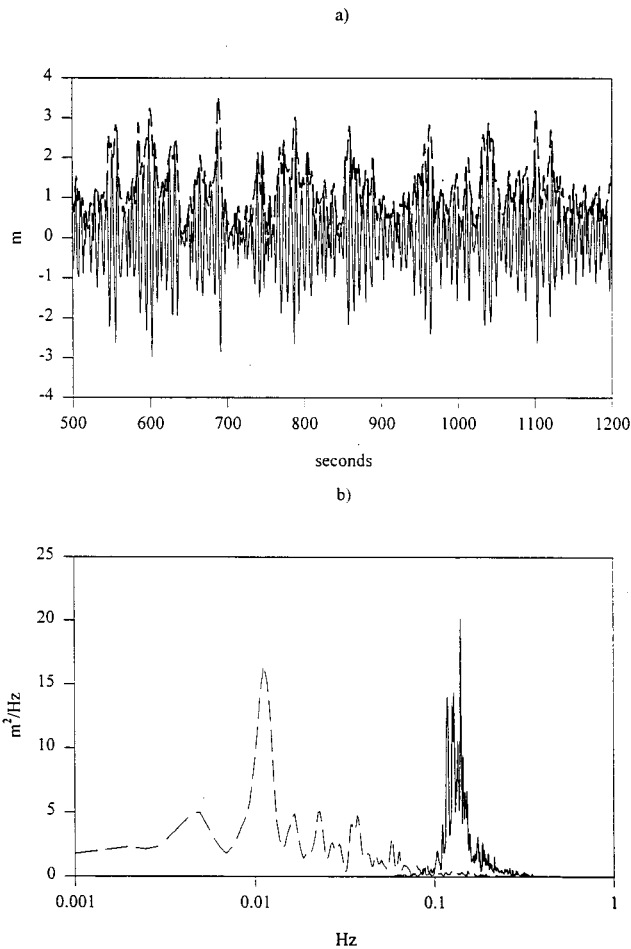


FIG. 15. (a) An example time series of the surface elevation (solid line) and the envelope function (dashed line) computed through the use of the Hilbert transform. Note the groupiness of the wave field, outlined by the wave envelope. (b) Computed power spectra of the surface wave heights (solid line) and the power spectra of the envelope function (dashed line). Distinct peaks occur at the peak of the wind wave spectrum at  $O(0.1)$  Hz while the wave group frequency appears to have a peak at  $O(0.01)$ .

sults suggest that the 99% contour depth has a characteristic length that scales with the wave amplitude rms.

### V. FINE SCALE PROPERTIES OF SOUND-SPEED FIELD

In order to appreciate the nature of the sound-speed field at smaller time scales, it is helpful to analyze the raw time series that were obtained at the 2-Hz rate. To qualitatively compare the data, color images of the sound-speed time series are used to show the behavior of the vertical sound-speed field. Figure 14 shows time series of the sound-speed field during the storm that peaks near year day 355, 1993 and whose mean depth profiles are shown in Fig. 11. The storm was chosen as representative of the typical response of the sound-speed field to increasingly rough conditions during a storm cycle. Each color image represents 40 min of data and panels are separated by approximately 4.5 h. At the onset of the storm, the reductions appear to be limited to the very near-surface region as shown in Fig. 14(a). As the seas develop, the scales of breaking increase, as displayed in the subsequent time series. The data shown in Fig. 14(b) dem-

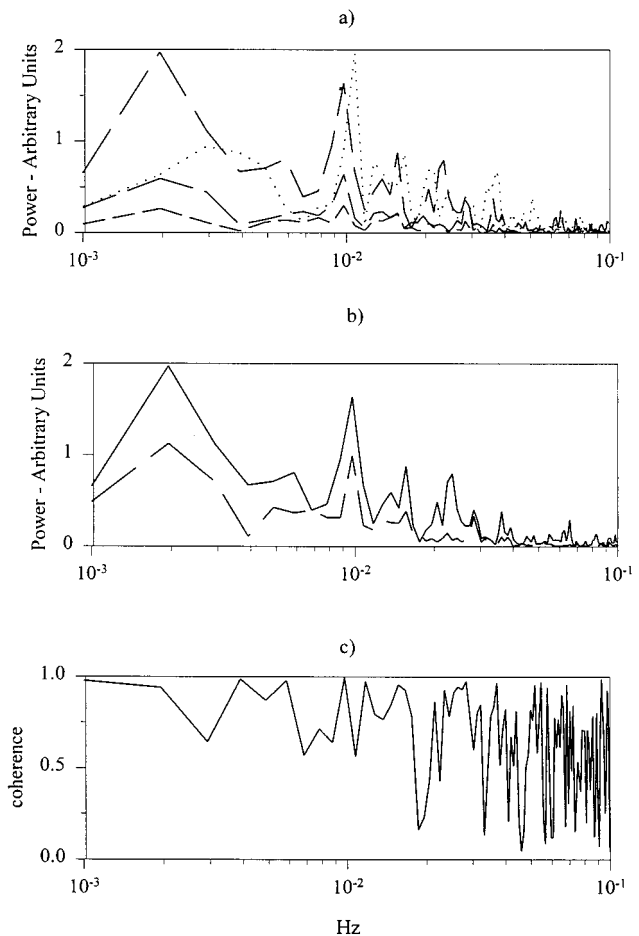


FIG. 16. (a) Spectra of the sound-speed field obtained from the shallowest three measurements and the spectra of the wave envelope (long dash—0.7 m, medium dash—1.0 m, short dash—1.6 m, dotted line—wave envelope). Good agreement between the spectra appears at  $O(0.01)$  Hz, the peak of the wave envelope spectrum. Vertical axis linear. (b) Spectra of the sound speed measured at 0.7 m (solid line) and the contour representing the depth (dashed line) at which the sound speed is 90% of the bubble-free value ( $\beta \cong 10^{-5}$ ). Vertical axis linear. (c) Computed coherence between the contour depth and sound-speed measured at 0.7 m. High coherence exists between the two at the lower wave group frequencies.

onstrate the effect of larger scale wave breaking injecting air to depth. Also apparent in the figure are the near-surface reductions that occur more frequently and persist for longer times. At the peak of the storm [Fig. 14(c)], the winds are in excess of 16 m/s and the significant wave heights approach 5 m. At this stage, the data reveal a persistent layer of reduced sound speed on which the deeper reductions are superimposed. Figure 14(b)–(e) show the response of the sound-speed field after the storm has peaked and begins to decay.

The large sound-speed reductions visible in Fig. 14(c), while variable in depth of penetration and residence time, appear to occur with some periodicity. To investigate the coupling of the wave field to the sound speed, the time series from the pitch-roll buoy are analyzed. The sea-surface elevation time series that corresponds with the sound-speed field shown in Fig. 14(c) is presented in Fig. 15(a). The low-frequency modulation of the wave field reflects the presence of wave groups or trains of high amplitude waves. A number of linear and nonlinear theories have been

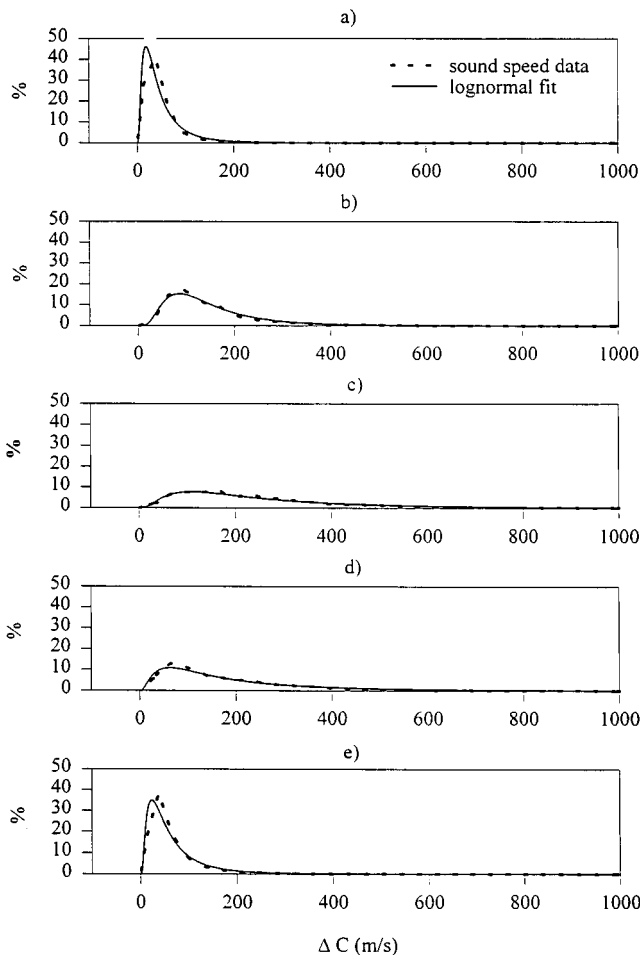


FIG. 17. Measured probability distributions (solid line) of the sound-speed reductions measured at 0.7 m during the storm shown in Fig. 11 and Fig. 14(a)–(e). A log-normal distribution (dotted line), based on the mean and variance of the signal is plotted with the data, providing good agreement over the course of the storm. Note the spreading of the distribution at the peak of the storm (c).

reviewed<sup>44,45</sup> that effectively describe the groupiness of the wave field. The envelope of the wave groups can be computed through application of the Hilbert transform.<sup>46,47</sup> If a complex time series  $S(t)$  is formed

$$S(t) = \eta(t) + iH[\eta(t)], \quad (6)$$

where the surface displacement time series is denoted by  $\eta(t)$  and  $H[\ ]$  is the Hilbert transform, the envelope of the displacement will be the magnitude of the complex signal,  $|S(t)|$ . This envelope is represented by the dashed line in Fig. 15(a). The corresponding power spectra of both the displacement and envelope signal are shown in Fig. 15(b), displaying distinct peaks for both the wind-wave spectrum  $O(0.1)$  Hz and for the envelope spectrum at  $O(0.01)$  Hz. A comparison between the envelope spectrum and the spectra of the near-surface sound-speed measurements obtained at the shallowest depths is shown in Fig. 16(a). The figure presents good agreement between the peak of the wave group spectrum and peaks in the sound-speed spectra at the lower group frequencies of  $O(0.01)$  Hz. Other comparisons between the wave envelope spectrum and the sound-speed field produce similar results during the various storm events over

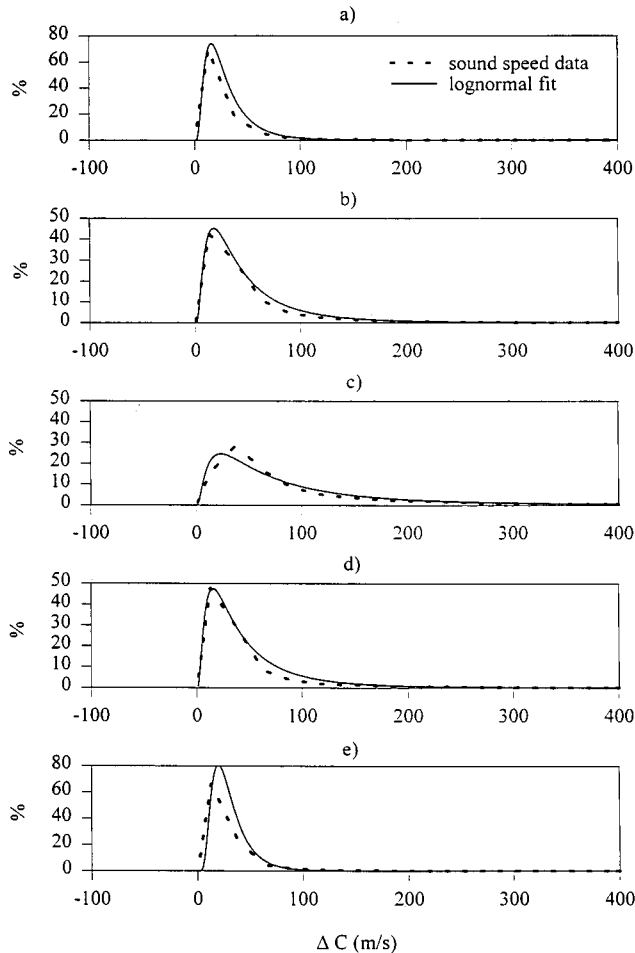


FIG. 18. Similar to Fig. 17(a)–(e) except the observed distributions are based on data obtained at the 1-m depth. Again, good agreement occurs between the predicted lognormal distribution (dotted line) and the data (solid line).

the course of the experiment. Clearly the data suggests a correspondence between the groupiness of the wave field and the frequency of the large sound-speed reductions. This is consistent with aerial observations of the appearance of whitecaps by Donelan, Longuet-Higgins, and Turner.<sup>48</sup>

The depth of the injection events is evaluated through analysis of the response of the contour depth which represents the depth at which the sound speed is 90% of the bubble-free sound speed. This contour was selected (void fraction  $\beta \approx 10^{-5}$ ) as its depth typically ranged from 1 to 3 m during these conditions ( $U_{10} = 16$  m/s,  $H_{1/3} = 5$  m). This depth range was chosen for the vertical resolution of the sound-speed module spacing. The spectrum of the depth of this layer is compared with the spectrum of the near-surface sound-speed measurement [Fig. 16(b)]. Agreement is evident between the two spectra at the lower wave group frequencies. The data indicates that the modulation of the penetration depth coincides with large sound-speed reduction events measured at the shallowest depth. Furthermore, the high levels of coherence between the near-surface sound speed and the contour depth [Fig. 16(c)], especially at the lower wave group frequencies, highlight the significance of the wave field in controlling not only the frequency of injection events, but the penetration of high bubble concentrations.

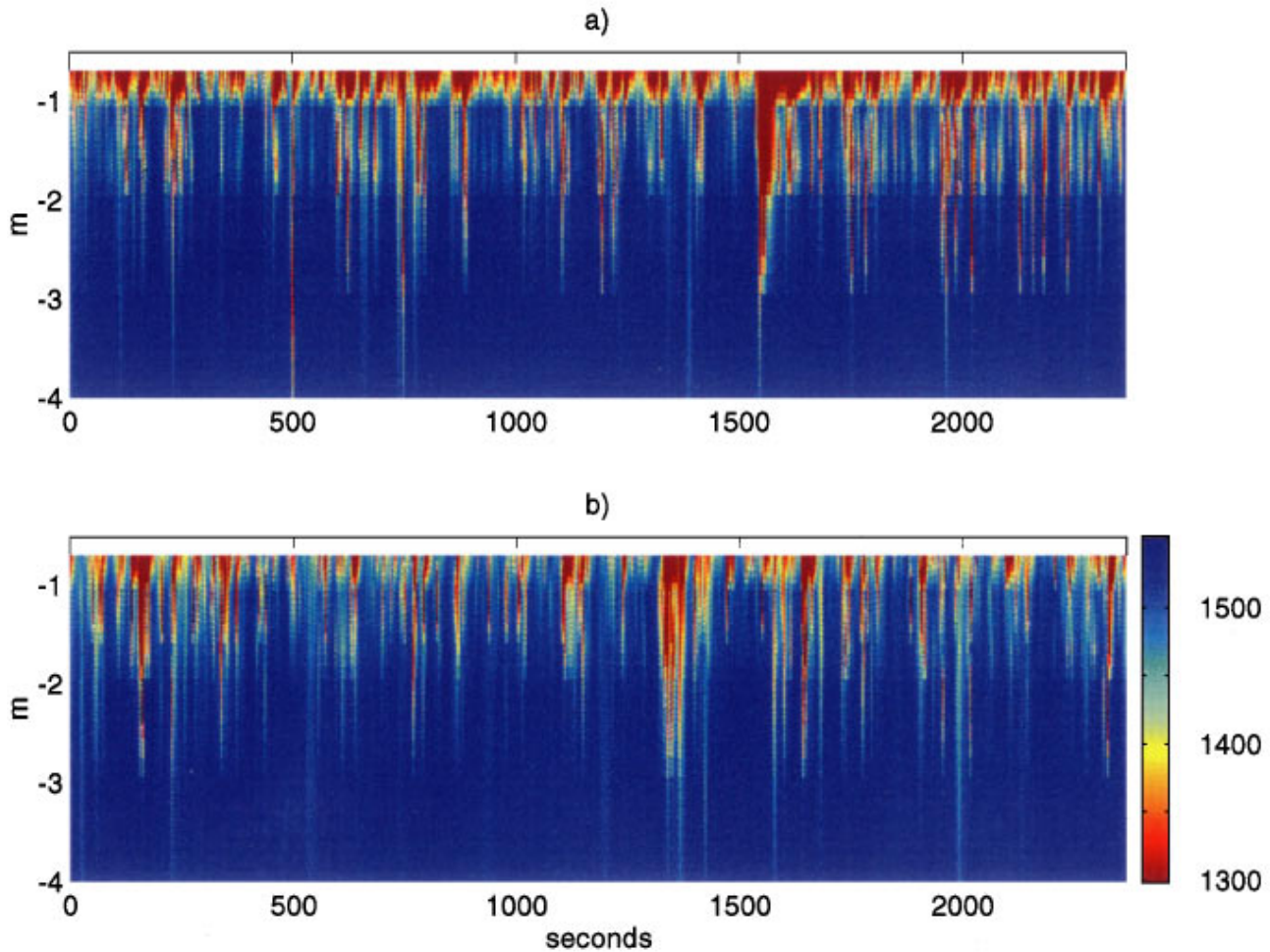


FIG. 19. Color contour plots of sound-speed time series during the peak of a storm occurring (a) 1993 year day 370 and (b) 1993 year day 380. While both time series exhibit the large, penetrating air injection events, the later storm (b) appears to lack a permanent layer of reduced sound speed just near the surface.

Figure 16(a) and (b) also shows evidence of a significant signal in the sound-speed and penetration depth at a frequency of  $2 \times 10^{-3}$  Hz. This does not appear to be associated with surface effects (although there is an unexplained peak in the envelope spectrum at  $3 \times 10^{-3}$  Hz) but may be associated with quasi-periodic Langmuir circulations. It is now well known that the lower-frequency modulation of acoustic backscatter measured by surface sonars at grazing incidence is dominated by scattering from bubbles entrained into Langmuir circulations.<sup>49</sup> The measurements reported here demonstrate that much of the variance associated with bubble-field parameters may be directly related to wave phenomena, rather than indirectly through Langmuir circulations, although both may play a role.

The probability distribution for the sound-speed reductions at 0.7- and 1-m measurement depths are shown in Figs. 17 and 18 for the previously discussed storm. The distributions are formed from the 40 min records using histograms with 25 m/s bins. Also shown are the corresponding log-normal distributions, based on the means and variances of the signals. During periods of intense wave breaking, the distribution spreads, indicating more occurrences of larger sound-speed reductions. At the beginning and the end of the storm, the distributions narrow, indicating fewer large reductions. Eventually, the distribution asymptotes to a delta func-

tion representing bubble-free water indicative of calm seas. Comparison between the two depths reveals that the deeper depth provides a narrower distribution, implying that the largest reductions occur closest to the surface. The trends in both the data and the calculated log-normal distributions appear to be in close agreement during periods of breaking throughout the 43-day record, and appear to extend to depths of approximately 3 m during high sea states. During calm periods, or at depths where there is little variation in the sound-speed signal, the agreement between the lognormal distribution and the data begin to deviate significantly.

A feature of the average data that deserves attention is the seemingly suppressed response of the sound-speed field to the storm that occurs near year day 380, 1993 (refer to Fig. 8). The suppression is evident when comparing the average sound speed during the storm to averages of earlier storms. A number of instrumentation issues were investigated in an attempt to determine if the differences were due to measurement errors. Effects of biofouling, low battery power, and buoy motion were considered, but provided no clear explanation for the apparent differences in the later storm cycle. In an effort to resolve the differences, color contours of the sound-speed field are created for the peaks of a number of storms. Figure 14(c) and Fig. 19(a) and (b) show the sound-speed field during storms under similar wind-

speeds. A common feature between the three storms is the presence of deep, intermittent sound-speed reductions that tend to persist for  $O(30)$  s, similar to the reduction shown in Fig. 6. These are the reductions that appear to vary at frequencies similar to the group frequencies of the surface wave field. A visible difference between the storm late in the experiment, Fig. 19(b), and the earlier storms [Figs. 19(a) and 14(c)], is a diminished near-surface layer of reduced sound speed.

If the frequent, shallow injection of air is attributed to the breaking of smaller scale waves, the suppressed response of the sound-speed field to the storm of 1993 day 380 suggests a decline of these smaller breakers during this period. One explanation for the suppressed small scale breaking is the drop in the magnitude of the surface currents at this time [Fig. 7(c)]. The elevated surface currents earlier in the record are due to the passage of an eddy that spun off the nearby Gulf Stream. Since the magnitude of the current is the same order of magnitude as the phase speed of higher-frequency wind waves [ $O(0.5-2)$ Hz], it is feasible that breaking of waves in these frequencies would be highly variable, dependent not only on the magnitude of the wind and current but the relative directions of the two. Observations have also shown that the penetration depths of bubble clouds are sensitive to stability of the surface waters.<sup>1</sup> In order to substantiate these effects, additional measurements would be required with an independent measurement of wave breaking. For example, the combination of video measurements of whitecap coverage and near-surface acoustic techniques, as well as measurements of water column stability, would provide the necessary data to further understand these processes.

## VI. DISCUSSION AND CONCLUSION

This paper reports on the results from the ASREX field experiment during which direct sound-speed measurements were acquired over a wide range of oceanographic conditions. A specialized buoy was designed and built which provided an autonomous platform from which direct sound-speed measurements could be made for an extended period. The data provide insight into the highly variable sound-speed field.

The wind speed provides strong correlations with the mean and rms sound speeds for wind speeds greater than approximately 8 m/s at the measurement depth closest to the surface. At the measurement depth of 1.6 m, the wind speed correlation appears robust, extending to lower wind speeds. The differences between the two depths indicate the variability of the entrainment of air in the shallow surface layer. As expected, comparisons of the mean and rms sound speeds with the significant wave height produced significant scatter, supporting previous work that indicates that the significant wave height may not be the best indicator of wave breaking at the ocean surface.

A parameter measuring the steepness of the wave field is calculated from data obtained from a pitch-roll buoy and correlated with the mean and rms sound-speed values. The computed steepness parameter provides the basis for a considerably improved correlation compared with the correlations of wind speed and significant wave height. Further evi-

dence for the dependence of air injection on the wave field is provided in the comparisons of the wave group frequencies and the frequency of sound-speed reductions. Analysis of the sound-speed time series reveals large injection events that last for  $O(30)$ s at periods similar to those which correspond to the wave groups. The depth of the contour which represents the depth at which the sound speed is 90% of the bubble-free sound speed is also found to modulate at similar frequencies. Lower-frequency modulations may be due to bubble transport by Langmuir circulations or low-frequency modulation of the wave envelope by distant swell.

It was found that Phillips<sup>36</sup> wave dissipation model, based on the wind and wave fields over the course of the experiment, gave significant correlations with both the mean and rms sound-speed measurements. It is anticipated that similar bulk dissipation estimates may be used for predicting other near-surface acoustic processes that are affected by wave breaking. Further refinements to the dissipation estimate, perhaps by inclusion of swell and current interactions, may better address the variability of the near-surface layer.

Despite contrasts in their measurement techniques and results, the previous field work by Lamarre and Melville<sup>25</sup> and Farmer and Vagle<sup>22</sup> found that an exponential function described the depth dependence of the sound-speed anomaly. The application of the exponential sound-speed depth profile is due in part to earlier work by Thorpe<sup>1,2</sup> and the fact that the low-frequency sound-speed reduction is proportional to void fraction for  $\beta < 10^{-5}$ . Modeling the vertical transport of bubbles using a turbulent transport model, Thorpe obtains an exponential profile when the diffusion coefficient is assumed to be constant with depth. The suggestion of a power-law dependence, specifically an inverse square profile, was made by Buckingham<sup>50</sup> in his work on bubble-generated acoustic waveguides. While the inverse square profile was initially suggested as a means to provide agreement between mode-filtering theory and observations of ambient noise below bubble clouds, a more physically based explanation has recently been proposed by Buckingham.<sup>51</sup>

The ASREX data set suggests that power laws in the range  $-2$  to  $-4$  describe the depth profiles. Recent measurements in the near-surface layer<sup>52,43</sup> show that levels of turbulent dissipation are one to two orders of magnitude higher than levels predicted by the previously accepted ideas of a wall turbulent boundary layer. In light of the variability in the ASREX data set and recent dissipation measurements, it is clear that a better knowledge of the near-surface turbulence is needed to give better turbulent transport models of bubbles.

The bulk of the effort presented here has been in the analysis of the 3.33-kHz sound-speed data. This was due in part to the fact that the lowest frequency we measured would best approximate the low-frequency/nondispersive limit. However, a brief discussion of the sound-speed data from the other two frequencies is warranted. Preliminary analysis of the 5- and 10-kHz data over the storm cycle discussed earlier (year day 355, 1993), provides evidence that the dispersive effects of bubbles may extend to frequencies as low as 5 kHz. Figure 20 presents time series of the mean sound speeds measured at (b) 0.7 m and (c) 1.6 m for all three

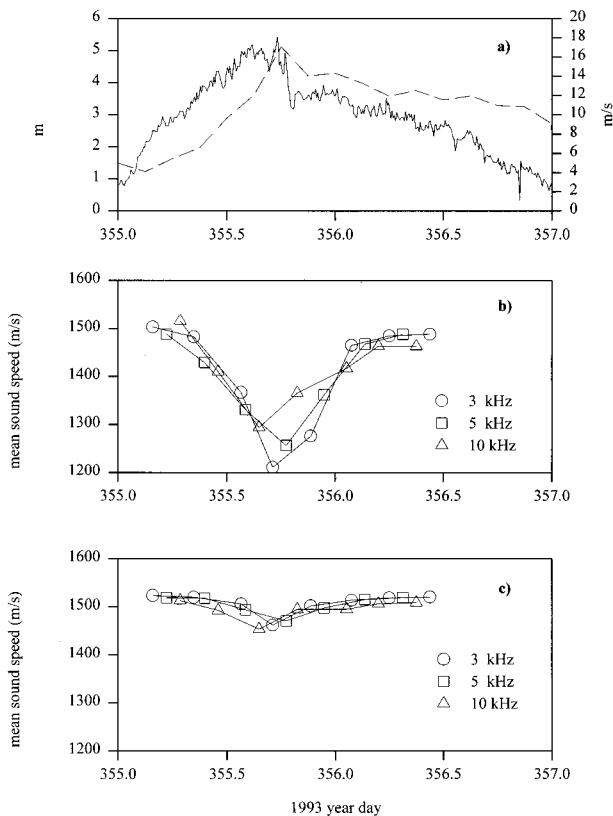


FIG. 20. Response of the sound-speed field over the course of a storm showing the effects of dispersion (year day 355, 1993). Times series show (a) significant wave height (dashed line) and wind speed (solid line) and the mean sound speed for 3.33, 5, and 10 kHz at the (b) 0.7-m and (c) 1.6-m measurement depths.

frequencies during the storm. While the measurements are not concurrent (a separation of 50 min between the end of one frequency and beginning of another), the means appear to track quite well together at the beginning of the storm. At the shallowest measurement, the means appear to deviate near the peak of the storm (~day 355.5). These deviations may be explained by a significant increase in bubbles of radii that resonate at or near 5 kHz ( $a_r \approx 650 \mu\text{m}$ ) during this time. Data from the deeper measurement do not appear to support this trend. However, it would be expected that fewer larger bubbles would exist at greater depths due to buoyancy effects and breakup mechanisms, resulting in the nondispersive limit shifting to higher frequencies.

## ACKNOWLEDGMENTS

The authors are indebted to a number of people whose professionalism led to the success of the ASREX project. We thank the officers and crew of both the R/V KNORR and R/V EDWIN LINK for providing a safe working environment for the deployment and recovery of the various moorings. The success of the moorings is due to the design and deployment by John Bouthiette, John Kemp, George Tupper, and Bryan Way of WHOI. We thank Bob Weller and Anand Gnanadesikan from WHOI and GFDL for providing the wave and meteorological data and Russ Davis from SIO for loaning the buoy floatation and tower. This project was funded by ONR (ARSRP and Acoustics).

- <sup>1</sup>S. A. Thorpe, "On the clouds of bubbles formed by breaking waves in deep water and their role in air-sea gas transfer," *Philos. Trans. R. Soc. London, Ser. A* **304**, 155–210 (1982).
- <sup>2</sup>S. A. Thorpe, "The role of bubbles produced by breaking waves in supersaturating the near-surface ocean mixing layer with oxygen," *Ann. Geophys. (France)* **2**, 53–56 (1984).
- <sup>3</sup>W. M. Carey and D. Browning, "Low frequency ambient noise: measurements and theory," in *Sea Surface Sound*, edited by B. R. Kerman (Kluwer Academic, Dordrecht, 1988), pp. 361–376.
- <sup>4</sup>H. Medwin and M. M. Beaky, "Bubble sources in the Knudsen sea noise spectra," *J. Acoust. Soc. Am.* **86**, 1124–1130 (1989).
- <sup>5</sup>H. Medwin and A. C. Daniel, "Acoustical measurements of bubble production by spilling breakers," *J. Acoust. Soc. Am.* **88**, 812–40 (1990).
- <sup>6</sup>A. Prosperetti, "Bubble-related ambient noise in the ocean," *J. Acoust. Soc. Am.* **84**, 1042–1054 (1988).
- <sup>7</sup>M. R. Loewen and W. K. Melville, "An experimental investigation of the collective oscillations of bubble plumes entrained by breaking waves," *J. Acoust. Soc. Am.* **95**, 1329–1343 (1994).
- <sup>8</sup>F. S. Henyey, "Acoustic Scattering from ocean microbubble plumes in the 100 Hz to 2 kHz region," *J. Acoust. Soc. Am.* **90**, 399–405 (1991).
- <sup>9</sup>P. M. Ogden and F. T. Erskine, "An empirical prediction algorithm for low-frequency acoustic surface scattering strengths," Naval Research Laboratory, Washington DC, 1992.
- <sup>10</sup>B. D. Johnson and R. C. Cooke, "Bubble populations and spectra in coastal waters: a photographic approach," *J. Geophys. Res.* **84**, 3761–3766 (1979).
- <sup>11</sup>A. L. Walsh and P. J. Mulhearn, "Photographic measurements of bubble populations from breaking wind waves at sea," *J. Geophys. Res.* **92**, 14553–14565 (1987).
- <sup>12</sup>M.-Y. Su, S. C. Ling, and J. Cartmill, "Optical microbubble measurement in the North Sea," in *Sea Surface Sound*, edited by B. R. Kerman (Kluwer, Dordrecht, 1988).
- <sup>13</sup>S. Baldy, "Bubbles in the close vicinity of breaking waves: statistical characteristics of the generation and dispersion mechanism," *J. Geophys. Res.* **93**, 8239–8248 (1988).
- <sup>14</sup>P. Geissler and B. Jahne, "A 3D-sensor for the measurement of particle concentration from image sequences," in *International Archives of Photogrammetry and Remote Sensing*, Vol. XXXI, Part B5, "Invited and Presented Papers of the XVIIIth Congress," Vienna, Austria, 9–19 July 1996, edited by P. Waldh (published by the Committee of the XVIII International Congress for Photogrammetry and Remote Sensing).
- <sup>15</sup>M. V. Hall, "A comprehensive model of wind generated bubbles in the ocean and predictions of the effects on sound propagation at frequencies up to 40 kHz," *J. Acoust. Soc. Am.* **86**, 1103–1117 (1989).
- <sup>16</sup>H. Medwin, "In situ acoustic measurements of bubble populations in coastal waters," *J. Geophys. Res.* **75**, 599–611 (1970).
- <sup>17</sup>H. Medwin, J. Fitzgerald, and G. Rautman, "Acoustic miniprobing for ocean microstructure and bubbles," *J. Geophys. Res.* **80**, 405–413 (1975).
- <sup>18</sup>H. Medwin, "In situ acoustic measurements of microbubbles at sea," *J. Geophys. Res.* **82**, 971–976 (1971).
- <sup>19</sup>H. Medwin and N. D. Breitz, "Ambient and transient bubble spectral densities in quiescent seas and under spilling breakers," *J. Acoust. Soc. Am.* **88**, 408–412 (1989).
- <sup>20</sup>M.-Y. Su, D. Todoroff, and J. Cartmill, "Laboratory comparisons of acoustic and optical sensors for microbubble measurement," *J. Atmos. Oceanic Tech.* **11**, 170–181 (1994).
- <sup>21</sup>S. Vagle and D. Farmer, "The measurement of bubble size distributions by acoustical backscatter," *J. Atmos. Oceanic Tech.* **9**, 630–644 (1991).
- <sup>22</sup>D. Farmer and S. Vagle, "Waveguide propagation of ambient sound in the ocean surface bubble layer," *J. Acoust. Soc. Am.* **86**, 1897–1908 (1989).
- <sup>23</sup>A. B. Wood, *A Textbook of Sound* (Bell, London, 1941).
- <sup>24</sup>C. S. Clay and H. Medwin, *Acoustical Oceanography* (Wiley, New York, 1977).
- <sup>25</sup>E. Lamarre and W. K. Melville, "Sound-speed measurements near the ocean surface," *J. Acoust. Soc. Am.* **96**, 3605–3616 (1994).
- <sup>26</sup>E. Lamarre and W. K. Melville, "Instrumentation for the measurement of sound speed near the ocean surface," *J. Atmos. Oceanic Tech.* **12**, 317–329 (1995).
- <sup>27</sup>E. Silberman, "Sound velocity and attenuation in bubbly mixtures measured in standing wave tubes," *J. Acoust. Soc. Am.* **29**, 925–933 (1957).
- <sup>28</sup>E. Lamarre, "An experimental study of air entrainment by breaking waves," Ph.D. thesis, MIT/WHOI Joint Program, 1993.
- <sup>29</sup>S. F. Barstow, G. Ueland, H. E. Krogstad, and B. A. Fossum, "The

- wavescan 2nd generation directional wave buoy," *IEEE J. Ocean Eng.* **16**, 254–266 (1991).
- <sup>30</sup>N. R. Galbraith, A. Gnanadesikan, W. M. Ostrum, E. A. Terray, B. S. Way, N. J. Williams, S. H. Hill, and E. Terrill, "Meteorological and Oceanographic Data during the ASREX III Field Experiment: Cruise and Data Report," WHOI technical Report No. 96-10, Woods Hole Oceanographic Institution, Woods Hole, MA.
- <sup>31</sup>H. Medwin, "Speed of sound in water: a simple equation for realistic parameters," *J. Acoust. Soc. Am.* **58**, 1318–1319 (1975).
- <sup>32</sup>F. Felizardo and W. K. Melville, "Correlations between ambient noise and the ocean surface wave field," *J. Phys. Oceanogr.* **25**, 513–532 (1995).
- <sup>33</sup>F. Felizardo, "Ambient Noise and Surface Wave Dissipation in the Ocean," Ph.D. thesis, MIT/WHOI Joint Program, Cambridge/Woods Hole, MA, 1993, 219 pp.
- <sup>34</sup>R. J. Rapp and W. K. Melville, "Laboratory measurements of deep-water breaking waves," *Philos. Trans. R. Soc. London, Ser. A* **331**, 735–800 (1990).
- <sup>35</sup>M. R. Loewen and W. K. Melville, "Microwave backscatter and acoustic radiation from breaking waves," *J. Fluid Mech.* **224**, 601–623 (1991).
- <sup>36</sup>O. M. Phillips, "Spectral and statistical properties of the equilibrium range in wind-generated gravity waves," *J. Fluid Mech.* **156**, 505–531 (1985).
- <sup>37</sup>K. Hasselmann, "On the spectral dissipation of ocean waves due to whitecapping," *Boundary-Layer Met.* **6**, 107–127 (1974).
- <sup>38</sup>G. J. Komen, S. Hasselmann, and K. Hasselmann, "On the existence of a fully developed wind-sea spectrum," *J. Phys. Oceanogr.* **13**, 816–827 (1984).
- <sup>39</sup>W. K. Melville, M. R. Loewen, F. C. Felizardo, A. T. Jessup, and M. J. Buckingham, "Acoustic and microwave signatures of breaking waves," *Nature (London)* **335**, 54–56 (1988).
- <sup>40</sup>R. M. Kennedy, "Acoustic radiation due to surface wave breaking," *J. Acoust. Soc. Am.* **94**, 2443–2445 (1993).
- <sup>41</sup>G. J. Komen, L. Cavaleri, M. Donelan, K. Hasselmann, S. Hasselmann, and P. A. E. M. Janssen, *Dynamics and Modeling of Ocean Waves* (Cambridge U.P., Cambridge, England, 1994), 532 pp.
- <sup>42</sup>W. K. Melville, "Energy dissipation by breaking waves," *J. Phys. Oceanogr.* **24**, 2041–2049 (1994).
- <sup>43</sup>W. K. Melville, "The role of surface-wave breaking in air–sea interaction," *Annu. Rev. Fluid Mech.* **28**, 279–321 (1996).
- <sup>44</sup>S. Elgar, R. T. Guza, and R. J. Seymour, "Groups of waves in shallow water," *J. Geophys. Res.* **89**, 3623–3634 (1984).
- <sup>45</sup>H. C. Yuen and B. M. Lake, "Instabilities of waves on deepwater," *Annu. Rev. Fluid Mech.* **12**, 303–334 (1980).
- <sup>46</sup>K. T. Shum and W. K. Melville, "Estimates of the joint statistics of amplitudes and periods of ocean waves using an integral transform technique," *J. Geophys. Res.* **89**, 6467–6476 (1984).
- <sup>47</sup>J. S. Bendat and A. G. Piersol, *Random Data: Analysis and Measurement Procedures* (Wiley, New York, 1986).
- <sup>48</sup>M. Donelan, M. S. Longuet-Higgins, and J. S. Turner, "Periodicity in whitecaps," *Nature (London)* **239**, 449–450 (1972).
- <sup>49</sup>A. J. Plueddemann, J. A. Smith, D. M. Farmer, R. A. Weller, W. R. Crawford, R. Pinkel, S. Vagle, and A. Gnanadesikan, "Structure and variability of Langmuir circulation during the Surface Waves Processes Program," *J. Geophys. Res.* **101**, 3525–3543 (1996).
- <sup>50</sup>M. J. Buckingham, "On acoustic transmission in ocean-surface wave guides," *Philos. Trans. R. Soc. London, Ser. A* **335**, 513–555 (1991).
- <sup>51</sup>M. J. Buckingham, "Sound speed and void fraction profiles in the sea surface bubble layer," *Appl. Acoust.* **51**, 225–250 (1997).
- <sup>52</sup>Y. C. Agrawal, E. A. Terray, M. A. Donelan, P. A. Hwang, A. J. Williams III, W. M. Drennan, K. K. Kahma, and S. A. Kitaigorodskii, "Enhanced dissipation of kinetic energy beneath breaking waves," *Nature (London)* **359**, 219–220 (1992).